Published October 7, 2013

Regulated vesicle fusion generates signaling nanoterritories that control T cell activation at the immunological synapse

Helena Soares,[1,2] Ricardo Henriques,[3,4] Martin Sachse,[5] Leandro Ventimiglia,[6] Miguel A. Alonso,[6] Christophe Zimmer,[3,4] Maria-Isabel Thoulouze,[1,2] and Andrés Alcover[1,2]

[1]Institut Pasteur, Department of Immunology, Lymphocyte Cell Biology Unit, F-75724 Paris, France
[2]Centre National de la Recherche Scientifique (CNRS) URA 1961, F-75724 Paris, France
[3]Institut Pasteur, Department of Cell Biology and Infection, Computational Imaging and Modeling Group, F-75724 Paris, France
[4]CNRS URA 2582, F-75724 Paris, France
[5]Institut Pasteur, Plateforme de Microscopie Ultrastructurale, Imagopole, F-75015 Paris, France
[6]Centro de Biología Molecular Severo Ochoa, Universidad Autónoma de Madrid (CSIC-UAM), Cantoblanco, 28049 Madrid, Spain

How the vesicular traffic of signaling molecules contributes to T cell receptor (TCR) signal transduction at the immunological synapse remains poorly understood. In this study, we show that the protein tyrosine kinase Lck, the TCRζ subunit, and the adapter LAT traffic through distinct exocytic compartments, which are released at the immunological synapse in a differentially regulated manner. Lck vesicular release depends on MAL protein. Synaptic Lck, in turn, conditions the calcium- and synaptotagmin-7–dependent fusion of LAT and TCRζ containing vesicles. Fusion of vesicles containing TCRζ and LAT at the synaptic membrane determines not only the nanoscale organization of phosphorylated TCRζ, ZAP70, LAT, and SLP76 clusters but also the presence of phosphorylated LAT and SLP76 in interacting signaling nanoterritories. This mechanism is required for priming IL-2 and IFN-γ production and may contribute to fine-tuning T cell activation breadth in response to different stimulatory conditions.

CORRESPONDENCE
Andrés Alcover:
andres.alcover@pasteur.fr
OR
Helena Soares:
helena.soares@pasteur.fr

Abbreviations used: dSTORM, direct stochastic optical reconstruction microscopy; MAL, myelin and lymphocyte; Syt7, synaptotagmin-7; TIRF, total internal reflection fluorescence.

T cell activation initiates the adaptive immune response and requires extracellular ligation of the TCR and the subsequent formation of dynamic signaling complexes. After TCR engagement, Lck phosphorylates its TCRζ subunit, enabling the recruitment and activation of ZAP70, which in turn phosphorylates the adapter LAT. Phosphorylated LAT acts as a scaffold, recruiting other adapters and effectors into multiprotein complexes driving downstream signal amplification and diversification, leading to T cell activation (Acuto et al., 2008). TCR signaling is sustained and regulated within a specialized cellular interface formed between a T cell and an antigen-presenting cell, the immunological synapse. Immunological synapse settings and function depend on both spatial cues and on the active transport of molecules to and within the synapse (Alcover and Thoulouze, 2010; Lasserre and Alcover, 2010).

M.-I. Thoulouze and A. Alcover contributed equally to this paper.

Compartmentalization in cells of the immune system facilitates the spatiotemporal organization of cellular responses essential for specialized immune functions. In T cells, TCR signal transduction relies on the compartmentalization of signaling molecules into plasma membrane nanodomains (Douglass and Vale, 2005; Lillemeier et al., 2010; Sherman et al., 2011). However, some molecules involved in TCR signaling do not just move on the plasma membrane, but must be transported across the T cell and delivered to the immunological synapse. Namely, the TCR, LAT, and Lck localize to vesicular compartments that are targeted to the immunological synapse upon TCR engagement (Ehrlich et al., 2002; Bonello et al., 2004; Das et al., 2004; Finetti et al., 2009). In resting T cells, Lck is constitutively active and distributes

The Rockefeller University Press $30.00
J. Exp. Med. 2013 Vol. 210 No. 11 2415-2433
www.jem.org/cgi/doi/10.1084/jem.20130150

Supplemental Material can be found at:
http://jem.rupress.org/content/suppl/2013/10/02/jem.20130150.DC1.html

Published October 7, 2013

between the plasma membrane and a vesicular compartment. Curiously, TCR triggering has no impact on the extent of Lck activity (Nika et al., 2010). This implies that Lck relocalization from its vesicular compartment to the immunological synapse may be responsible for TCR signal propagation. One important question raised by these findings concerns how the traffic of signaling molecules to specific regions of the plasma membrane is regulated to execute spatially restricted signaling.

Previous works put forward several traffic regulators involved in cytokine secretion and lytic granule release at CD4 (Huse et al., 2006) and CD8 (de Saint Basile et al., 2010) T cell synapses, respectively. However, it is unknown how the vesicular traffic of signaling molecules to the immunological synapse is regulated. TCR signal transduction might rely on endosomal traffic regulators and their specific subcellular localization. Validation of this concept requires the identification of Rab proteins and their effectors, which coordinate the transport and delivery of Lck, LAT, and TCRζ vesicles to the immunological synapse.

Here, we show that the regulated fusion of Lck, LAT, and TCRζ distinct vesicular compartments at the synapse determines the spatial organization, number, density, and molecular composition of its signaling nanoclusters, as well as the presence of signaling nanoterritories within phosphorylated LAT and SLP76 clusters. Lck acts as the signal switch and calcium acts as the mediator of a vesicle fusion positive feedback loop that builds a functional immunological synapse capable of driving T cell activation and cytokine production.

RESULTS

Lck, TCRζ, and LAT reside in distinct exocytic vesicular compartments

We assessed Lck, TCRζ, and LAT subcellular localization and traffic regulators to establish whether they trafficked in distinctly regulated vesicular compartments. Primary CD4 T and Jurkat cells (unpublished data) displayed a Lck intracellular compartment finely intermingled with those of LAT and TCRζ; however, co-localization was minimal (<3%), whereas TCRζ and LAT compartments co-localized to a higher, yet still feeble, extent (unpublished data).

The specification of the intracellular traffic route and the vesicular compartment identity rely on the Rab family GTPases (Fukuda, 2008). In turn, vesicle fusion is mediated by SNARE proteins whose function is restricted to precise subcellular microenvironments (Stojilkovic, 2005). To ascertain the identity of Lck, LAT, and TCRζ intracellular compartments, we looked into 19 Rabs and 1 SNARE that have both been linked either to regulated exocytosis or to the transport of endosomes to plasma membrane (Fukuda, 2008), and to a previously described protein for specialized transport, myelin and lymphocyte protein (MAL), which mediates Lck transport to the plasma membrane (Antón et al., 2008). We transiently expressed each Rab-GFP fusion protein in Jurkat cells and assessed their co-localization with respect to Lck, LAT, and TCRζ vesicular compartments. These signaling molecules localized in highly individualized compartments, with little to no overlap in their Rab specification (Fig. 1). Lck vesicular compartment co-localized (∼35%) with the recycling endosomal marker Rab11b and with MAL (∼23%; Antón et al., 2008; Fig. 1, D and H). LAT vesicular compartment co-localized with Rab27a (∼35%) and Rab37 (∼30%; Fig. 1, M and N), two Rab molecules known to regulate cytokine and cytotoxic granule exocytosis in $CD4^+$ and $CD8^+$ T cells, respectively (Stinchcombe et al., 2001; Huse et al., 2006). TCRζ peripheral vesicles co-localized to the fast recycling Rab4b compartment (∼8%), whereas its core co-localized to Rab3d- (∼25%) and Rab8b-regulated (∼30%) exocytic compartments (Huse et al., 2006; Fukuda, 2008; Fig. 1, Q–S). Noteworthy, the secretory v-SNARE protein Ti-VAMP (Chaineau et al., 2009) co-localized with both LAT (∼30%) and TCRζ (∼30%) vesicular compartments (Fig. 1, O and W).

LAT and TCRζ vesicular release is regulated by calcium and synaptotagmin-7

The traffic regulators present in LAT and TCRζ vesicles (Fig. 1) have been reported to be involved in stimulus-induced exocytosis at cytotoxic synapses (Ménager et al., 2007; Marcet-Palacios et al., 2008). To pinpoint the molecular mechanism regulating Lck, LAT, and TCRζ release from vesicular compartments, we assessed the role of calcium, a known regulator of stimulus-dependent exocytosis (Stojilkovic, 2005; Pang and Südhof, 2010). To increase cytosolic calcium levels, we treated CD4 T cells either with thapsigargin or ionomycin. To accurately quantify Lck, LAT, and TCRζ distribution between intracellular vesicles and the plasma membrane, we stained for surface CD2 and then used it to automatically segment the plasma membrane. The resulting automated mask delimiting the internal and external outlines of the plasma membrane allowed us to discriminate and quantify the subcellular distribution (plasma membrane versus vesicular compartment) of our proteins of interest (materials and methods; unpublished data). We found LAT and TCRζ distribution to the vesicular compartment to be higher than anticipated by others (Bonello et al., 2004), ∼75% (Fig. 2, A, B, H, and I). In fact, through plasma membrane segmentation, we were able to distinguish plasma membrane–resident LAT and TCRζ from their intracellular compartments and subcortical vesicles, within the limits of the confocal microscopy resolution (unpublished data). Lck displayed a higher plasma membrane distribution with ∼25% in intracellular vesicles (Fig. 2, C and J; and not depicted).

Consistent with LAT localization in Rab27a and Rab37 exocytic compartments, increased cytosolic calcium led to a clear release of its vesicular compartment into the plasma membrane (Fig. 2, A, I, and O; and not depicted). In agreement with TCRζ-segregated distribution into a Rab3d and Rab8b exocytic compartment and also into Rab4b rapid recycling endosomes, cytosolic calcium increase induced an incomplete release of TCRζ vesicular compartment (Fig. 2, D, K, and O; and not depicted). As expected from their presence in Rab11b and MAL compartments, neither thapsigargin nor ionomycin induced Lck vesicle release (Fig. 2, F, M, and O; and not depicted).

Thapsigargin effects on LAT and TCRζ exocytosis seem specific, rather than the consequence of the redistribution of

Published October 7, 2013

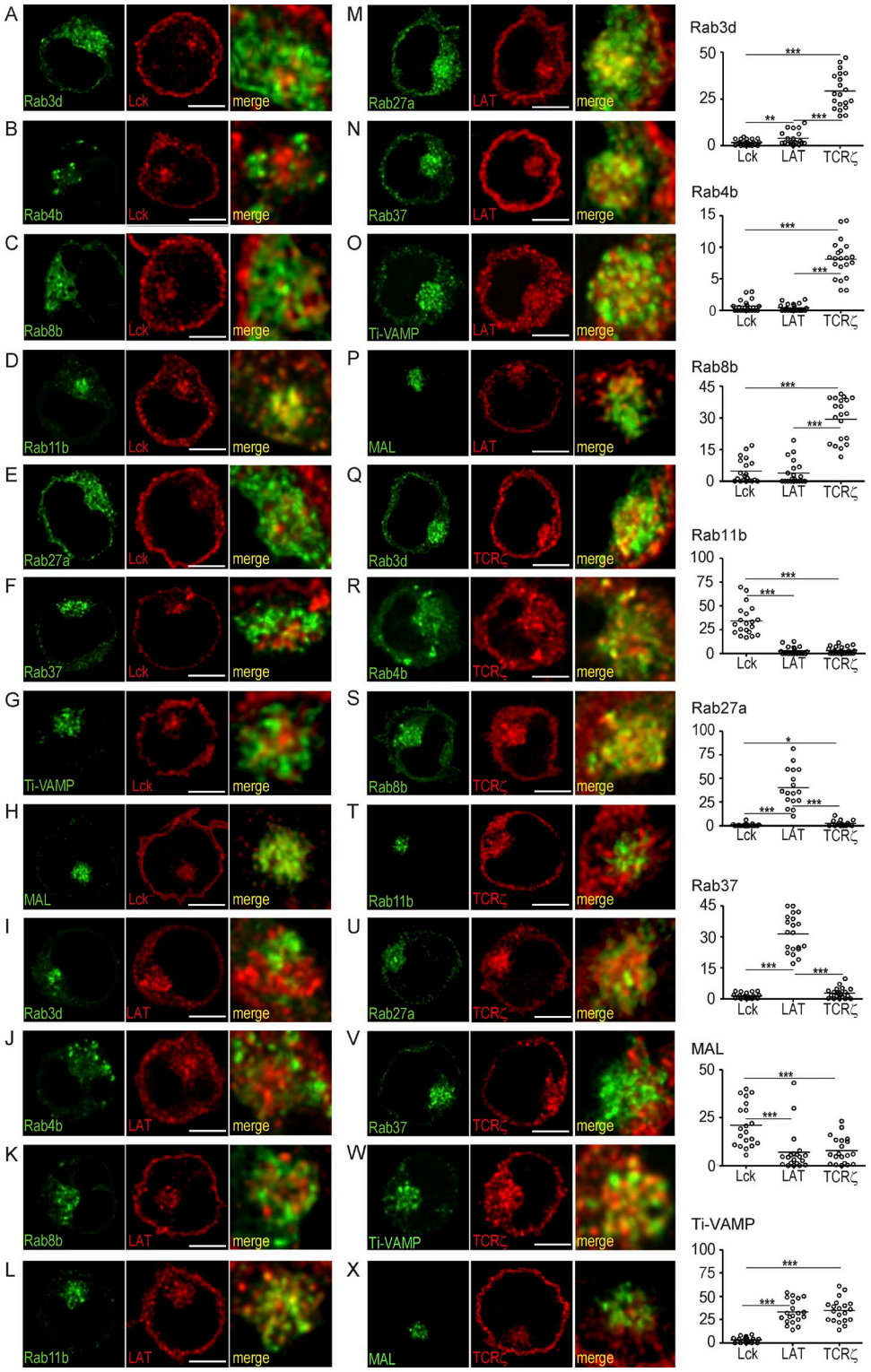

Figure 1. Lck, TCRζ, and LAT traffic through distinct exocytic compartments. Jurkat cells were transfected with GFP-tagged Rab3d (A, I, and Q), Rab4b (B, J, and R), Rab8b (C, K, and S), Rab11b (D, L, and T), Rab27a (E, M, and U), Rab37 (F, N, and V), Ti-VAMP (G, O, and W), and MAL (H, P, and X). Cells were then stained for Lck (A–H), LAT (I–P), and TCRζ (R–X). 3D confocal images were post-treated by deconvolution. A 1-µm-thick medial stack is shown. Right panels show a zoomed image of the vesicular compartment (frame). Plots in the far right column depict the population analysis of the co-localization volume between Lck, LAT, and TCRζ and each one of the traffic regulators analyzed for at least 20 cells per group. ***, $P \leq 0.0001$; **, $P \leq 0.01$; *, $P \leq 0.05$; Mann-Whitney test. Images representative of three experiments. Bar, 5 µm.

Published October 7, 2013

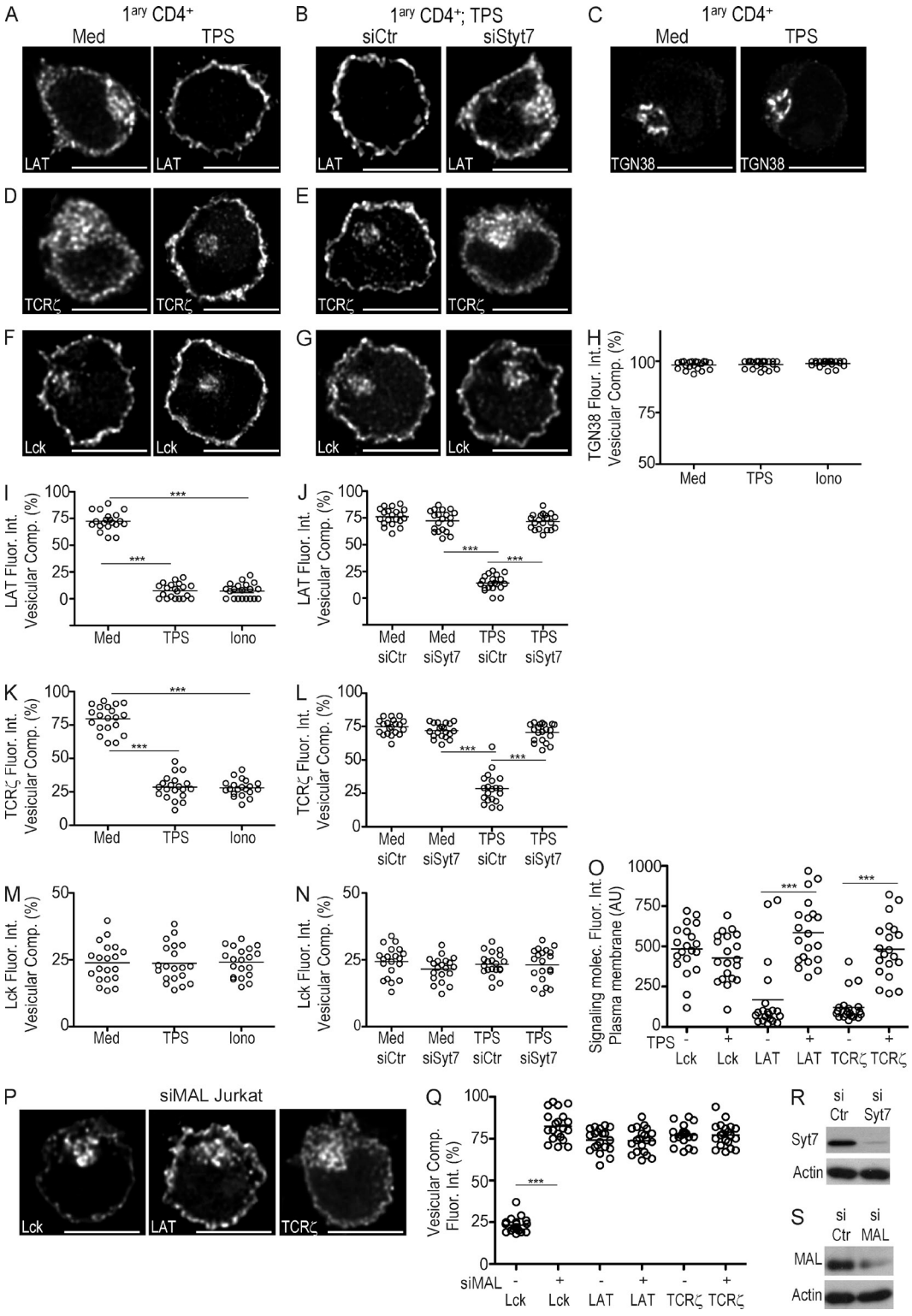

Figure 2. Intracellular calcium increase and Syt7 regulate the release of LAT and TCRζ from their vesicular compartments to the plasma membrane, whereas MAL specifically regulates Lck traffic. (A–G) Primary CD4 T cells were transfected with siRNA against Syt7, a nonrelevant sequence (siCtr), or left untransfected (Med) and then treated with 5 µM thapsigargin (TPS) for 30 min. Cells were stained for LAT (A and B), TGN38 (C), TCRζ (D and E), and Lck (F and G) and analyzed by 3D confocal microscopy. (H–N) Population analysis quantifying the 3D fluorescence intensity in the vesicular compartment (see Materials and methods) relative to total fluorescence of TGN38 (H), LAT (I and J), TCRζ (K and L), and Lck (M and N) of at least 20 cells per group processed as in A–G. (O) Population analysis of $n = 20$ cells per group quantifying Lck, TCRζ, and LAT localized at the plasma membrane in cells

Published October 7, 2013

multiple compartments, as neither the trans-Golgi network (TGN38$^+$) nor the endosomal-recycling compartment (transferrin receptor$^+$) were released by a cytosolic calcium raise (Fig. 2, C and H; and not depicted). There was no significant overlap of LAT with the biosynthetic compartment labeled by TGN38 (~5% co-localization; unpublished data). LAT's fast traffic through the secretory pathway might preclude its concentration required for detection.

Calcium-regulated exocytosis relies on the presence of vesicle-associated fusion proteins (v-SNARES) and calcium sensors (synaptotagmins; Pang and Südhof, 2010). LAT and TCRζ vesicular compartments displayed Ti-VAMP (Fig. 1, O and W), a v-SNARE known to interact with the calcium sensor synaptotagmin-7 (Syt7; Rao et al., 2004), suggesting Syt7 involvement in this process. Syt7-silencing in primary CD4 T cells did not alter LAT and TCRζ steady-state distribution (Fig. 2, J and L), or their distribution into the TGN38 compartment (not depicted), obviating any effects of Syt7 silencing on the constitutive fusion of the biosynthetic and endocytic pools of LAT and TCRζ to the plasma membrane. However, Syt7 silencing impaired TCRζ and LAT release from their vesicular compartments in response to increased cytosolic calcium levels (Fig. 2, B, E, J, and L). Single Syt7 siRNA oligonucleotides directed to distinct RNA sequences inhibited calcium-induced vesicular LAT release, albeit at a lesser extent than their combination, ruling out siRNA off-target effects (unpublished data).

The egress of Lck from vesicles into the plasma membrane requires MAL (Antón et al., 2008). Consistent with its specific distribution in Lck vesicles (Fig. 1, H, P, and X), MAL silencing led to an accumulation of Lck in the vesicular compartment (approximately threefold signal increase), without altering LAT or TCRζ steady-state distribution (Fig. 2, P and Q).

Therefore, Lck, LAT, and TCRζ vesicle traffic is regulated by distinct molecular mechanisms. Lck depends on MAL and is calcium-insensitive, whereas TCRζ and LAT vesicle release is induced by calcium and mediated by Syt7. Still, a fraction of the TCRζ compartment is not released in response to calcium. This may reflect the presence of TCRζ in the Rab4b rapid recycling compartment (Fig. 1 R).

Lck controls the release of TCRζ and LAT vesicular compartments to the immunological synapse

We next investigated how the differential regulation of Lck, LAT, and TCRζ vesicular compartments conditioned their targeting to the immunological synapse. We inhibited Lck traffic by silencing MAL expression, or TCRζ and LAT vesicle fusion by silencing Syt7, and analyzed 30-min synapses. Strikingly, MAL silencing prevented not only Lck, but also LAT and TCRζ vesicle release, and their full clustering at the synapse, although compartment polarization and an incipient TCRζ cluster were observed (Fig. 3, A–G). In contrast, Syt7 silencing inhibited LAT and TCRζ compartment delivery and synaptic clustering, without effecting Lck clustering. A residual TCRζ clustering was observed in Syt7-silenced cells (Fig. 3, L–O, arrowheads and arrows). Consistent with a calcium-dependent triggering of TCRζ and LAT vesicle fusion, intracellular calcium chelation by BAPTA abrogated TCRζ and LAT compartment release and clustering without significantly perturbing Lck synaptic clustering (unpublished data).

These data show that Lck, TCRζ, and LAT vesicle release at the synaptic membrane is differentially regulated. The inhibitory effect of MAL silencing on LAT and TCRζ vesicle fusion at the synapse, and the fact that it doesn't affect LAT and TCRζ steady-state traffic, suggests that previous Lck synaptic delivery is necessary for LAT and TCRζ vesicle fusion.

Lck-, TCRζ-, and LAT-regulated traffic is pivotal to TCR signal transduction at the immunological synapse

TCR signaling is mediated by formation of transient, heterogeneous clusters of signaling molecules whose structure and subcellular origin remain uncertain (Dustin and Depoil, 2011). Our experimental build-up provided us with the means to disentangle the contributions of regulated signaling molecule exocytosis for TCR signaling.

We inhibited Lck traffic through MAL-silencing, and TCRζ and LAT vesicle fusion through Syt7-silencing. We monitored specific phosphorylated tyrosine residues (pY), hallmarks of TCR signal transduction: the activatory pY^{394} of Lck, pY^{142} of TCRζ and pY^{191} of LAT. From now on, phosphorylated proteins will be designated by pLck, pTCRζ, and pLAT.

Consistent with their synaptic clustering patterns (Fig. 3, A–F), at 30 min of conjugate formation, the extent of pLck and pLAT clustered at synapses formed by MAL-silenced cells was strongly diminished (Fig. 4, A–H), although a partial pTCRζ cluster was observed (Fig. 4, F and I, arrows). Conversely, Syt7-silenced cells displayed normal pLck, very low pLAT, and residual pTCRζ clustering at the synapse (Fig. 4, J–R).

These data indicate that the juxtaposition of vesicular LAT to an immunological synapse displaying fully clustered pLck is not enough for LAT phosphorylation to occur. Instead, LAT synaptic phosphorylation requires the prior clustering of Lck at the synapse, as well as the calcium and Syt7-dependent synaptic fusion of vesicular LAT.

untreated (−), or treated with TPS (+) for 30 min and processed as in A–G. (P) Jurkat cells were transfected with siRNA against MAL or a nonrelevant sequence (siCtr). Cells were stained for LAT (middle), TCRζ (right), and Lck (left) and analyzed by 3D confocal microscopy. (Q) Population analysis of $n = 20$ cells per group, quantifying Lck, LAT, and TCRζ in the vesicular compartment relative to total cellular fluorescence (see Materials and methods) in MAL-silenced cells (siMAL$^+$) compared with control (siMAL$^-$), treated as in P. (R and S) Syt7, MAL, and actin (control) levels in primary CD4 T cells transfected with siRNA control (siCtr), siRNA Syt7 (siSyt7), or siRNA MAL (siMAL). Cell lysates were analyzed by Western blot. Confocal images were post-treated by deconvolution. A 1-µm-thick medial stack is shown. Each dot in plots represents one cell. ***, $P \leq 0.0001$; **, $P \leq 0.01$; *, $P \leq 0.05$; Mann-Whitney test. Images representative of three experiments. Bar, 5 µm.

Published October 7, 2013

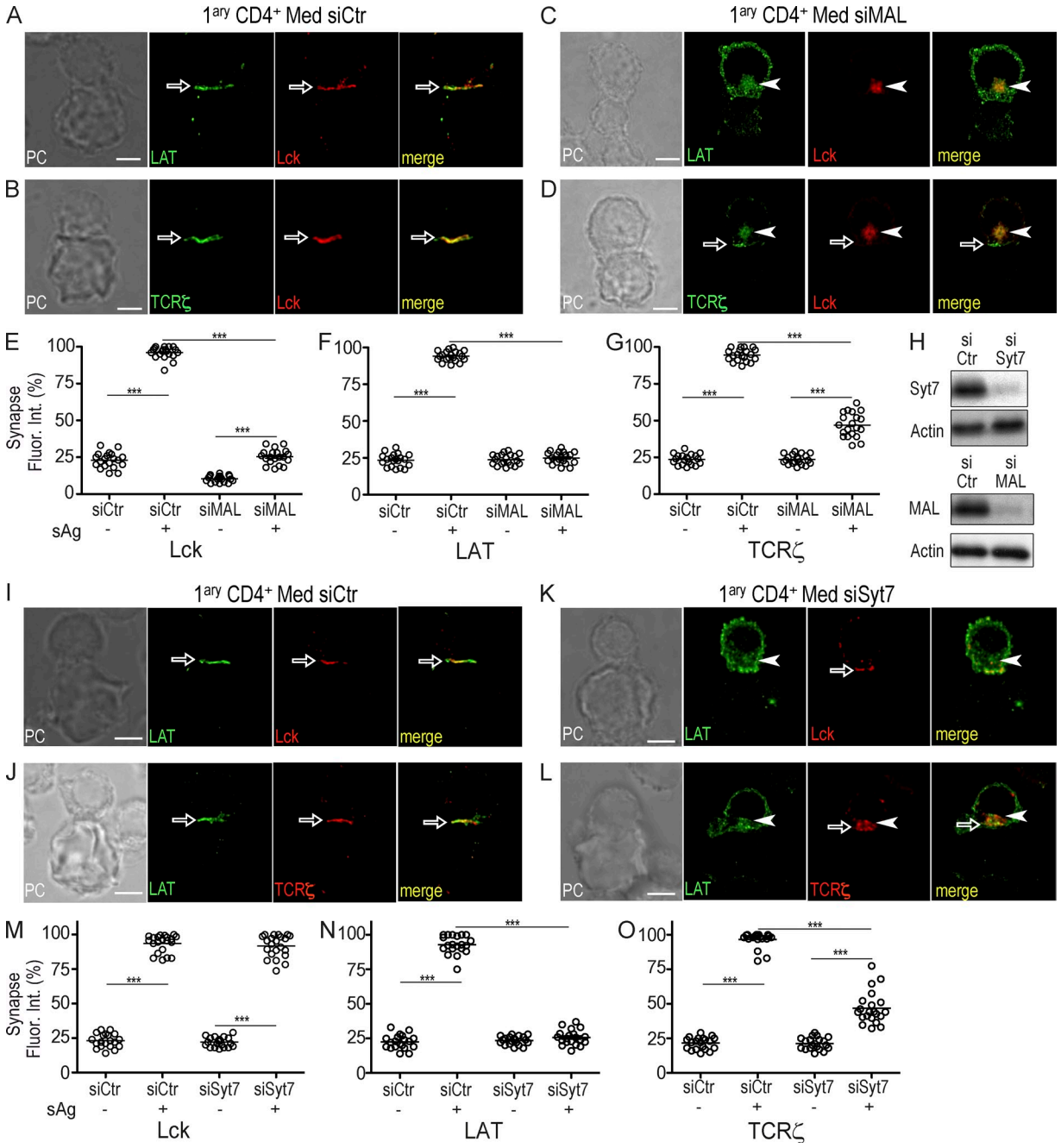

Figure 3. Lck instructs LAT and TCRζ vesicular release at the immunological synapse. (A–D) Primary CD4 T cells were transfected with a siRNA control (siCtr; A and B) or a siRNA MAL (siMAL; C and D) and allowed to form immunological synapses with superantigen-loaded Raji cells for 30 min. Cells were stained for Lck and LAT (A and C) or Lck and TCRζ (B and D), and then analyzed by 3D confocal microscopy. (E–G) Population analysis of at least 20 conjugates per group quantifying the 3D fluorescence at the synapse relative to total cell fluorescence in cells processed in the same way as cells in A–D in the presence (sAg^+) or in the absence (sAg^-) of superantigen. (H) Primary CD4 T cells were transfected with siRNA control (siCtr), siRNA MAL (siMAL), or siRNA Syt7 (siSyt7) and cell lysates were analyzed for MAL, Syt7, and actin expression by Western blot. (I–L) Primary CD4 T cells were transfected with a siRNA control (siCtr; I and J) or a siRNA Syt7 (siSyt7; K and L) and allowed to form immunological synapses with superantigen-loaded Raji cells for 30 min. Cells were stained for Lck and LAT (I and K) or LAT and TCRζ (J and L). (M–O) Population analysis of at least 20 conjugates per group, quantifying the 3D fluorescence at the cell junction relative to total cell fluorescence in cells processed in the same way as cells in I–L and activated in the presence (sAg^+) or in absence (sAg^-) of superantigen and analyzed by 3D confocal microscopy. Confocal images were post-treated by deconvolution and 1 µm-thick medial stack is shown. Synaptic clustering and intracellular compartments are highlighted by arrows and arrowheads, respectively. Each dot in plots represents one conjugate. ***, $P \leq 0.0001$; **, $P \leq 0.01$; *, $P \leq 0.05$; Mann-Whitney test. Images are representative of three experiments. Bar, 5 µm.

Published October 7, 2013

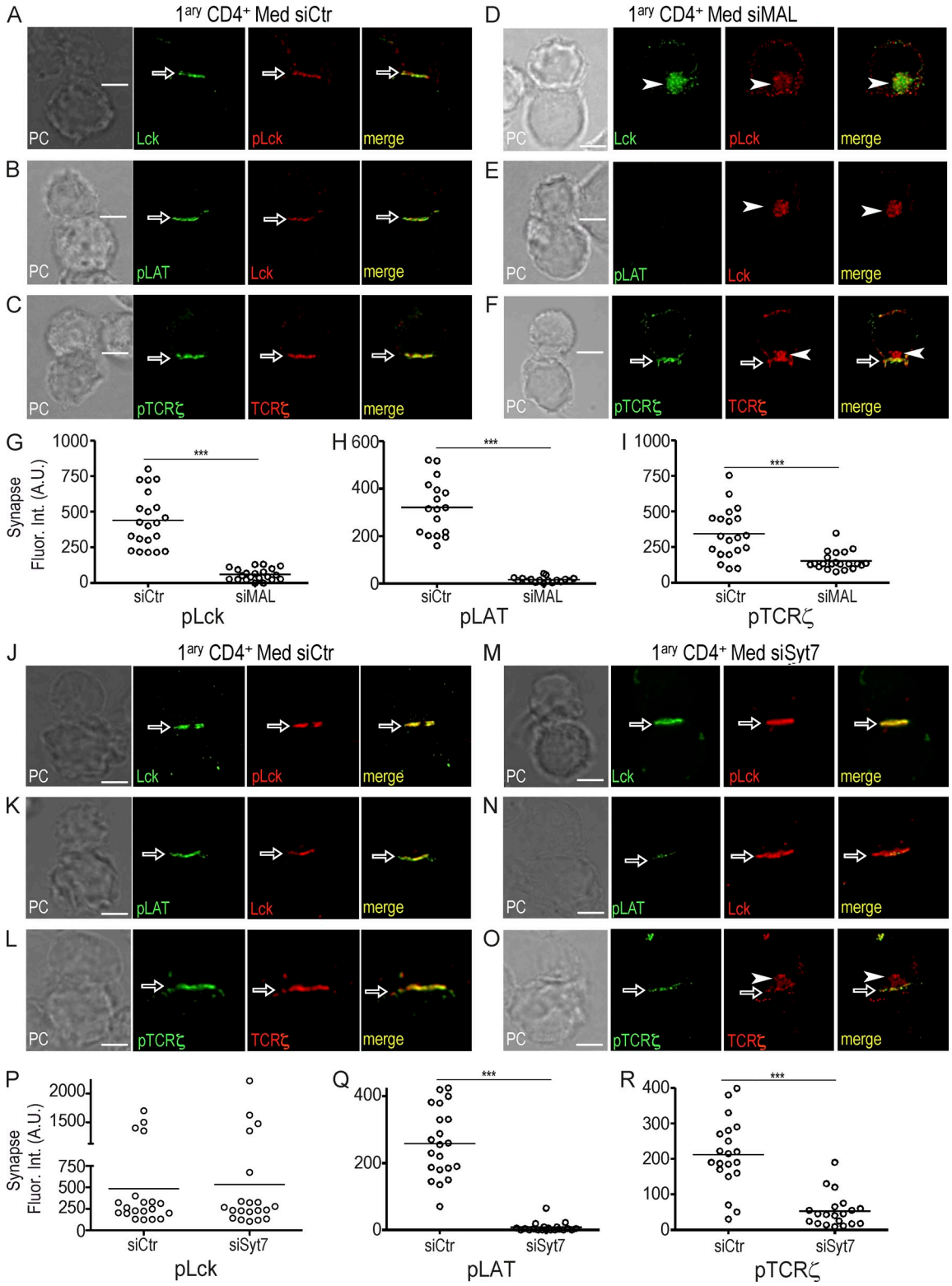

Figure 4. LAT and TCRζ vesicle fusion at the immunological synapse is required for signal amplification. (A–F) Primary CD4 T cells were transfected with a siRNA control (siCtr; A–C) or a siRNA MAL (siMAL; D–F), and allowed to form conjugates with superantigen-loaded Raji cells for 30 min. Cells were stained for Lck and pLck (A and D), Lck and pLAT (B and E), or TCRζ and pTCRζ (C and F) and analyzed by 3D confocal microscopy. (G–I) Population analysis of primary CD4 T cells transfected with siRNA control (siCtr), or siRNA MAL (siMAL) of pLck (G), pLAT (H) and pTCRζ (I) fluorescence intensity at the immunological synapse of at least 20 conjugates per group. (J–O) Primary CD4 T cells were transfected with a siRNA control (siCtr; J–L) or siRNA Syt7 (siSyt7; M–O) and allowed to form conjugates with superantigen-loaded Raji cells. Cells were stained for Lck and pLck (J and M), Lck and pLAT (K and N),

Published October 7, 2013

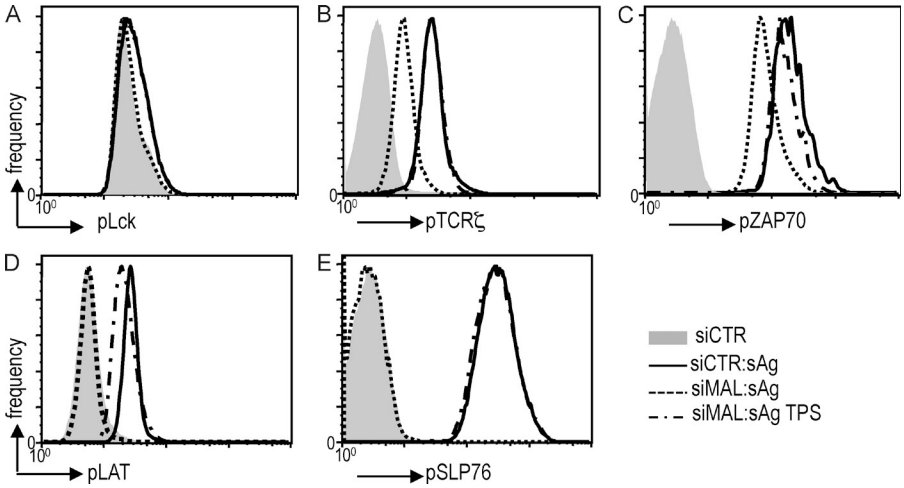

Figure 5. Effect of MAL-silencing on TCRζ, ZAP70, LAT, and SLP76 phosphorylation levels. (A–E) Primary CD4 T cells were transfected with a siRNA control (siCtr; J–L), or siRNA MAL (siSyt7; M–O) and allowed to form conjugates with superantigen-loaded Raji cells for 30 min. Cells were stained pLck (A), pTCRζ (B), pZAP70 (C), pLAT (D), or pSLP76 (E), and cellular levels were determined by intracellular fluorescence cytometry. Representative of two experiments.

MAL silencing differentially affects Lck, TCRζ, ZAP70, LAT, and SLP76 phosphorylation

Our previous findings raised the question of how the regulated traffic and fusion of vesicle-associated Lck, LAT, and TCRζ determine TCR signaling. To further investigate the effect of hindering Lck traffic on early TCR signaling, MAL-depleted cells were activated for 30 min with superantigen-pulsed Raji cells in the presence or absence of thapsigargin. The presence of specific phosphotyrosine residues was assessed by intracellular flow cytometry.

Consistent with a previous report (Nika et al., 2010), Lck phosphorylation was not affected either by MAL silencing or TCR engagement (Fig. 5 A). In contrast, LAT and SLP76 phosphorylation were fully inhibited in MAL-silenced cells (Fig. 5, D and E), whereas TCRζ and ZAP70 phosphorylation were partially inhibited (Fig. 5, C and E). Thapsigargin treatment of MAL-silenced cells restored TCRζ, ZAP70, LAT, and SLP76 phosphorylation levels.

These data indicate that synaptic Lck sets the threshold for the calcium and Syt7-mediated TCRζ and LAT vesicle release that controls pTCRζ and pLAT clustering and the subsequent recruitment of pZAP70 and pSLP76.

TCRζ and ZAP70 signaling organization is mildly affected by MAL silencing

Our aforementioned findings raised the question of how the regulated traffic and fusion of vesicle-associated Lck, TCRζ, and LAT determine TCR signal organization at the synaptic membrane. Hence, we inhibited vesicle traffic or fusion and analyzed, at high spatial resolution, the distribution of early (i.e., pTCRζ, pZAP70) and amplification (i.e., pLAT, pSLP76) signaling complexes, at high spatial resolution.

We performed two-color direct stochastic optical reconstruction microscopy (dSTORM) combined with total internal reflection fluorescence (TIRF; Heilemann et al., 2008) on fixed cells. dSTORM super-resolution microscopy accurately localizes single molecules (see Materials and methods) and allowed us to quantify different parameters of the plasma membrane signaling organization, including the presence of protein clusters, their size, relative density, and abundance. In addition, we coupled 3D wide-field imaging to our dSTORM imaging apparatus to monitor for the presence of LAT vesicular compartment, by expressing a GFP-tagged LAT (Fig. 6; boxes, top left).

MAL silencing lead to mild differences in pTCRζ and pZAP70 nanocluster organization, with a small reduction in pTCRζ numbers and cluster area (Fig. 6, B, F, and H) and to an enrichment in small pZAP70 clusters (dimers and trimers; Fig. 6, B and I). No changes were observed in nanocluster density or shape (Fig. 6, J–M).

TCRζ and LAT vesicle fusion determine pLAT nanocluster organization and their ability to recruit pSLP76

Current models for TCR signaling issued from biochemical approaches and standard light microscopy propose the generation of an amplification signalosome formed by direct association of pLAT and pSLP76–Gads complexes (Acuto et al., 2008). Thus, we monitored the spatial distribution of pLAT and pSLP76 at the immunological synapse. We observed important differences in pLAT and pSLP76 nanocluster distribution under different activation conditions. Anti-CD3 stimulation (αCD3) led to a significant increase in the number and relative density of both pLAT and pSLP76 clusters, compared with nonstimulated cells spread on anti-CD45 (αCD45; Fig. 7, A and E; and Fig. 8, A–D). Inhibition

or TCRζ and pTCRζ (L and O) and analyzed by 3D confocal microscopy. (P–R) Population analysis of pLck (P), pLAT (Q), and pTCRζ (R) fluorescence intensity at the synapse of at least 20 conjugates per group, processed as in J–O. Confocal images were post-treated by deconvolution. A 1-µm-thick medial stack is shown. Synaptic clustering and intracellular compartments are highlighted by arrows and arrowheads, respectively. Each dot in plots represents one conjugate. . ***, $P \leq 0.0001$; **, $P \leq 0.01$; *, $P \leq 0.05$; Mann-Whitney test. Images are representative of three experiments. Bar, 5 µm.

Published October 7, 2013

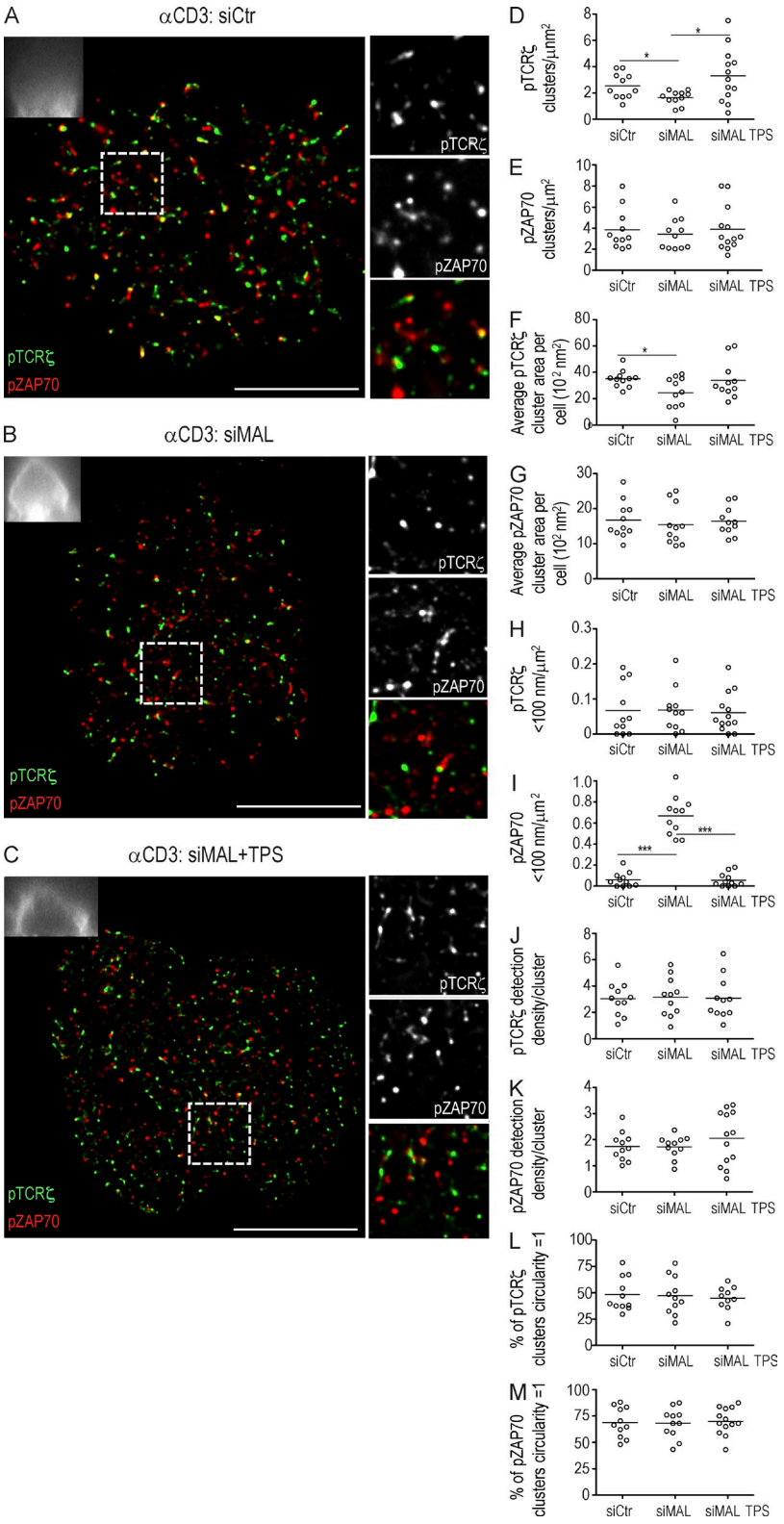

Figure 6. Effect of MAL-silencing on TCRζ and ZAP70 recruitment and phosphorylation at the immunological synapse. (A–C) Jurkat cells were transfected with either siCtr (A), or siMAL (B and C) in the absence (A and B) or the presence (C) of thapsigargin and allowed to spread for 3 min on an αCD3-coated coverslips. Cells were stained for pTCRζ and pZAP70 and analyzed by dSTORM-TIRF imaging. Top left insets depict the correspondent zx-stack widefield image projection of GFP-TCRζ. Right panels show a magnified image of a region of interest (frame). pTCRζ, green; pZAP70, red. (D–L) Population analysis in Jurkat cells processed as in A–C (n = 11) of the number of pTCRζ or pZAP70 clusters per square micrometer (D and E), the mean pTCRζ or pZAP cluster area per cell (F and G), the number of pTCRζ or pZAP70 clusters <100 nm for each cell analyzed (H and I), the number of pTCRζ or pZAP70 detections per individual cluster for each cell analyzed (J and K), and the percentage of clusters whose circularity is equal to one. Value is given by the ratio between the largest and the smallest feret diameters for all the clusters detected and plotted as the mean for each analyzed cell (L and M). Images representative of three experiments. ***, $P \leq 0.0001$; **, $P \leq 0.01$; *, $P \leq 0.05$; Mann-Whitney test. Each circle represents a cell. Bar, 10 μm.

of TCRζ and LAT compartments synaptic fusion, directly through Syt7-, or indirectly through MAL-silencing, caused a twofold reduction in pLAT and pSLP76 cluster number, size and relative density to levels of nonstimulated cells (αCD45). This was accompanied by a significant shift toward smaller clusters and a concomitant decrease in the number and particle density of pSLP76 clusters (Fig. 7; and Fig. 8, A–E).

Published October 7, 2013

To disentangle the effect of blocking Lck traffic on LAT phosphorylation, from its effect on vesicular LAT synaptic fusion, we blocked the calcium-insensitive Lck traffic through MAL silencing and provoked the calcium-sensitive fusion of vesicular TCRζ and LAT. Thapsigargin treatment of MAL-silenced cells lead to the release of LAT vesicular compartment and a concomitant increase in the number, relative density and area of pLAT clusters which displayed increased ability to recruit pSLP76 clusters when compared with MAL-silenced cells. Interestingly, promoting TCRζ and LAT vesicular fusion through thapsigargin treatment of MAL-silenced cells is sufficient to recover a number and density of pLAT clusters similar to the one observed in activatory synapses (Fig. 7; and Fig. 8, A and C).

These results indicate that, first, Lck-deficient clustering at the synapse creates a signaling bottleneck caused by the impaired synaptic delivery of vesicular TCRζ and LAT, and second, once vesicular LAT is delivered at the synapse, even reduced amounts of synaptic Lck are apt to extensively phosphorylate LAT clusters, if not as comprehensively (Fig. 8, C and E).

The contribution of vesicular TCRζ and LAT to the synapse nanoscale organization went beyond an effect in the number and density of pLAT clusters, it also affected their morphology.

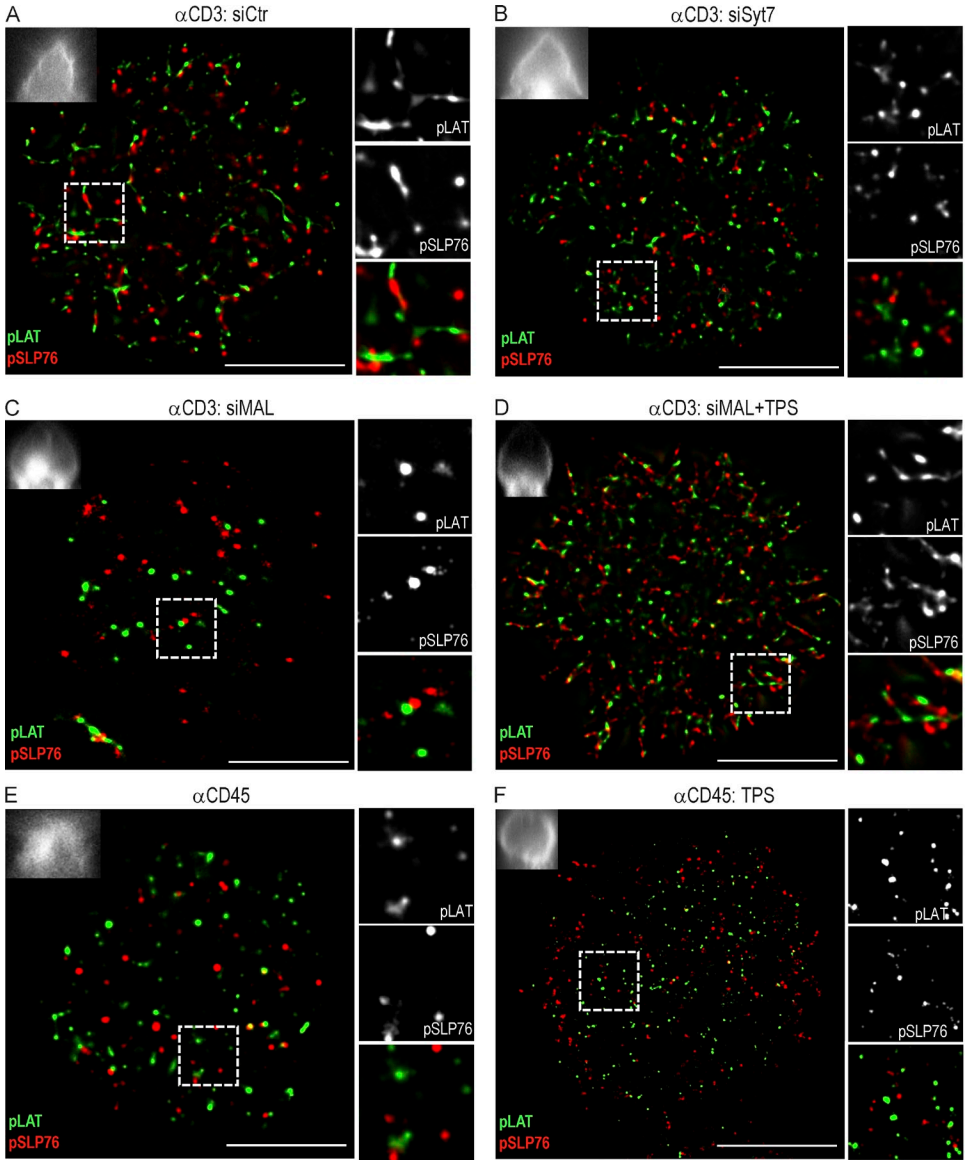

Figure 7. LAT vesicle fusion determines pLAT and pSLP76 nanoscale organization at the immunological synapse. (A–F) Jurkat cells were transfected with siCtr (A), siSyt7 (B), or siMAL (C and D) in the absence (A–C and E) or presence (D and F) of thapsigargin, and allowed to spread for 3 min on an αCD3- (A–D) or αCD45-coated (E and F) coverslip. Cells were stained for pLAT and pSLP76 and analyzed by dSTORM-TIRF imaging. Top left insets depict the correspondent zx-stack widefield image projection. Right panels show a magnified image of a region of interest (frame). pLAT in green, pSLP76 in red. Images are representative of three experiments. Bar, 10 µm.

Published October 7, 2013

αCD3-stimulated control cells displayed a population of larger and elongated pLAT nanoclusters, which were adjacent to pSLP76 clusters (Fig. 7 A; and Fig. 8 F). In contrast, upon LAT compartment retention, the majority of pLAT nanoclusters were circular, as in nonstimulated cells (Fig. 7, B, C, and E). Elongated pLAT clusters (~20 μm²) are the main contributors to the increase in pLAT cluster size in αCD3-stimulated cells (Fig. 8 G). Reinforcing the role of LAT vesicle fusion in the spatial organization of signaling complexes, thapsigargin treatment of MAL-silenced cells elicited the appearance of the elongated pLAT clusters (Fig. 7 D; and Fig. 8 F). Thapsigargin-induced LAT vesicle fusion in αCD45-adhered cells did not recover pLAT nanoscluter organization, indicating that it depends on TCR stimulation (Fig. 7 F; and Fig. 8, A-F).

Our live imaging (Video 1) is consistent with a model whereby LAT vesicle delivery at the synapse occurs as soon as the cell contacts the activatory surface (15–45 s).The likely fusion of vesicle LAT at discrete synaptic locations (highlighted by arrows) originates the elongated LAT clusters (demarked by polygons) that are fed by LAT vesicles during the entire length of the acquisition (7 min mark). Due to spatial resolution limitations inherent to live imaging, our video microscopy interpretation was performed in light of the aforementioned super-resolution data.

These results suggest that pLAT clusters result from two subpopulations with distinct subcellular origins: the plasma membrane and the vesicular compartment. Moreover, the fact that pTCRζ and pZAP70 were mildly affected by Lck vesicle traffic inhibition indicates that TCR stimulation modulates the synapse nanoscale organization in a TCRζ and LAT vesicle fusion-dependent manner.

LAT vesicle fusion promotes pLAT and pSLP76 intermolecular proximity

Our data indicate that TCRζ and LAT vesicle fusion is key to generate the spatial organization of pLAT and pSLP76 nanoclusters in TCR-stimulated synapses. We investigated

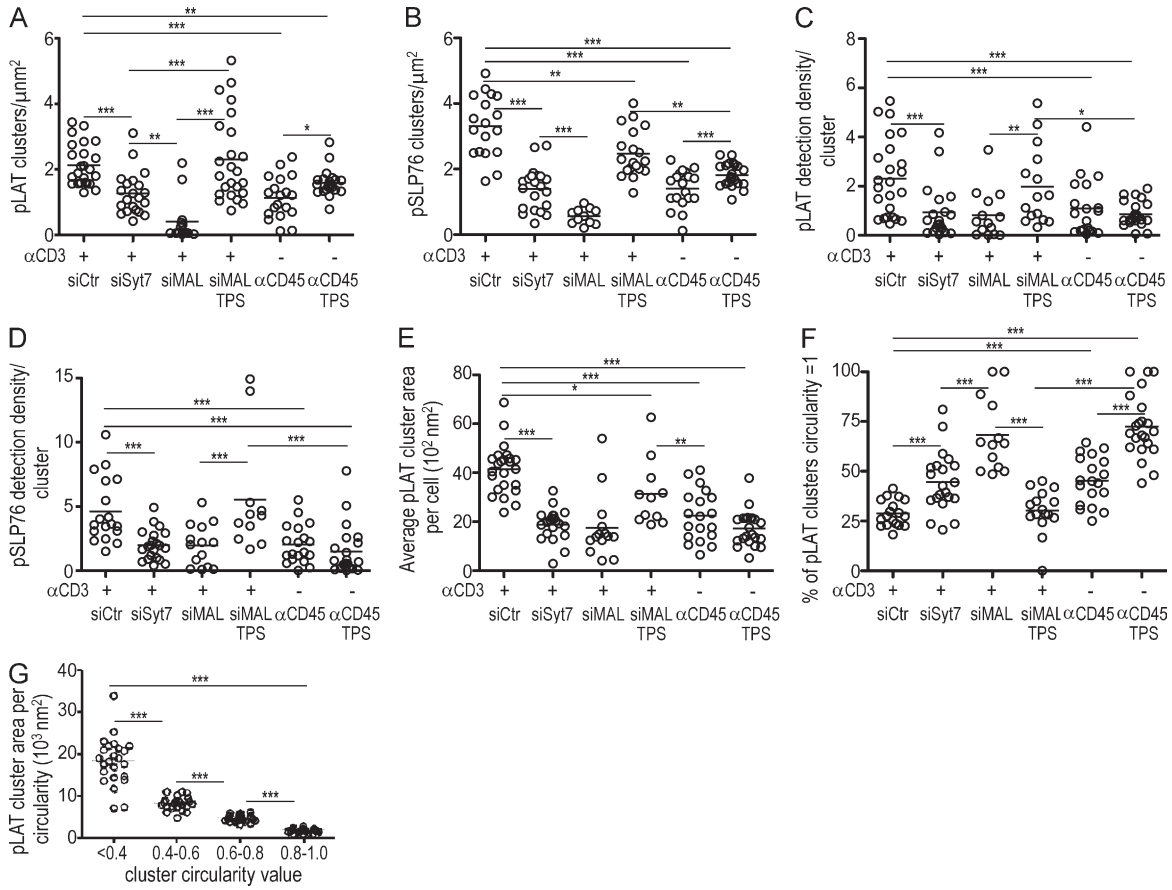

Figure 8. LAT vesicle fusion determines the number, density, and morphology of pLAT and pSLP76 nanoclusters at the immunological synapse. (A–G) Population analysis of pLAT and pSLP76 clusters in Jurkat cells processed as in Fig. 7. (A) Number of clusters per square micrometer is as follows: siCtr, $n = 24$; siSyt7, $n = 21$; siMAL, $n = 14$; siMAL TPS, $n = 11$; αCD45, $n = 20$; and αCD45 TPS, $n = 22$. (B) Number of clusters per square micrometer is as follows: siCtr, $n = 18$; siSyt7, $n = 21$; siMAL, $n = 14$; siMAL TPS, $n = 11$; αCD45, $n = 19$; and αCD45 TPS, $n = 22$. (C and D) Number of pLAT (C) and pSLP76 (D) detections per individual cluster for each cell analyzed for $n \geq 11$ cells. (E) Mean pLAT cluster area per cell, $n \geq 11$ cells. (F) Percentage of clusters whose circularity is equal to 1 per cell. Circularity value is given by the ratio between the large and the small feret diameters for all the clusters detected $n \geq 11$ cells. (G) Mean area of pLAT clusters per cell according to circularity, measured as in F ($n = 24$). ***, $P \leq 0.0001$; **, $P \leq 0.01$; *, $P \leq 0.05$; Mann-Whitney test. Each circle represents a cell. Representative of three experiments.

Published October 7, 2013

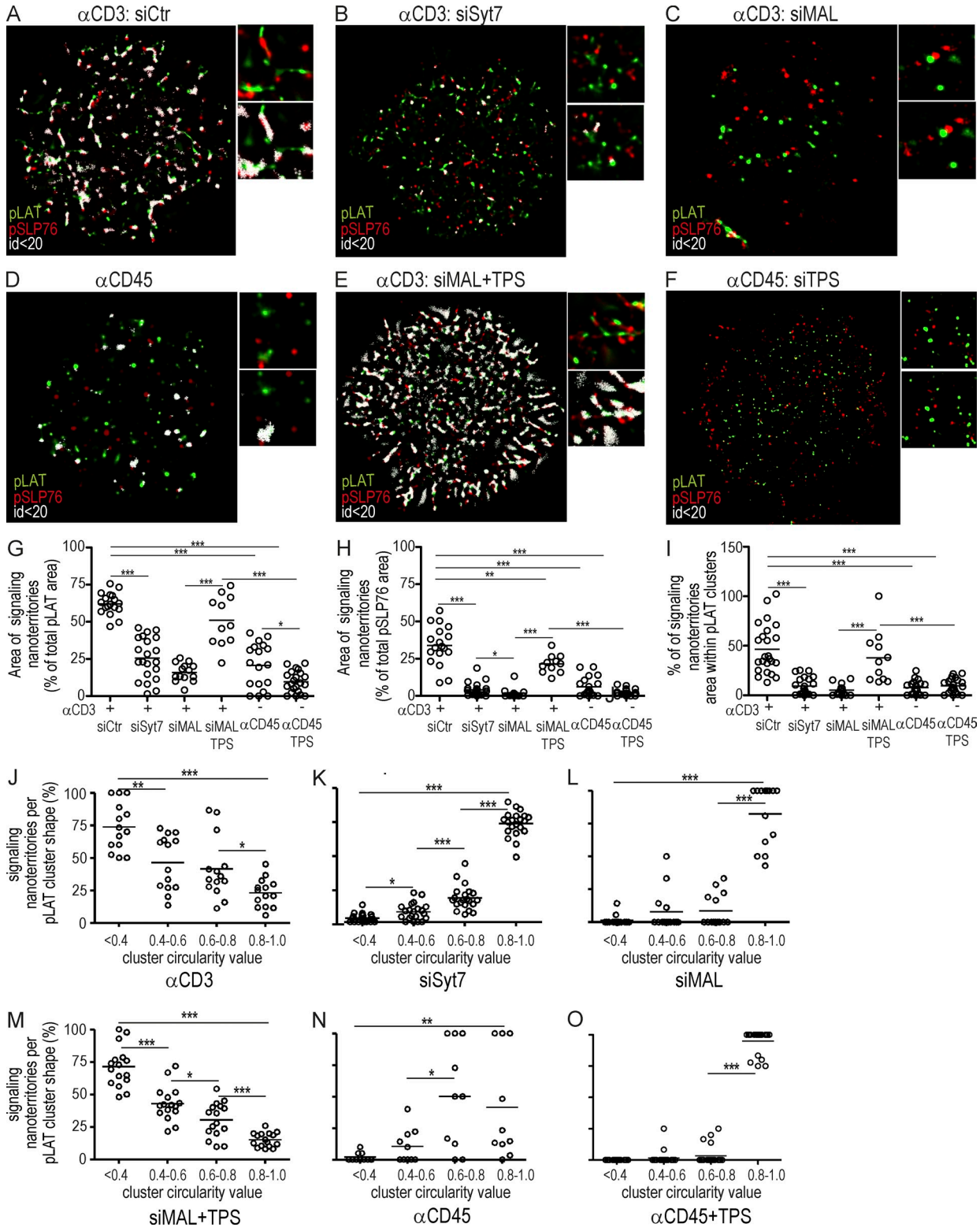

Figure 9. Vesicle fusion generates pLAT synaptic clusters at interacting distances from pSLP76 clusters: signaling nanoterritories. (A–F) Jurkat cells were transfected with siCtr (A), siSyt7 (B), or siMAL (C and E) in the absence (A–D), or presence (E and F) of thapsigargin, and allowed to spread for 3 min on an αCD3- (A–C and E) or αCD45-coated (D and F) coverslips. Cells were stained for pLAT and pSLP76 and analyzed by dSTORM-TIRF imaging. Right panels show a magnified image of a region of interest (frame). pLAT, green; pSLP76, red; pLAT and pSLP76 detections that are distant to each other by less than 20 nm (signaling nanoterritories), white. (G–O) Population analysis of pLAT and pSLP76 signaling nanoterritories in Jurkat cells processed as in A–F. (G–H) Mean percentage per cell of the area occupied by signaling nanoterritories with respect to the total pLAT (G) and pSLP76 (H). (G) Number of

Published October 7, 2013

whether this nanocluster organization could correlate with increased interactions between these two adapters, and thus with enhanced TCR signal amplification (Acuto et al., 2008).

In agreement with previous super-resolution studies (Lillemeier et al., 2010; Sherman et al., 2011), we found that pLAT and pSLP76 clusters appeared contiguous, but only mildly overlapped (Fig. 7 A), indicating that pLAT and pSLP76 do not interact extensively. This raises the possibility that pLAT and pSLP76 interactions could be occurring in spatially discrete locations. To address this hypothesis, we developed a method to identify possible pLAT and pSLP76 interactions, independent of their molecular concentration. To do so, we mapped the locations where pLAT and pSLP76 molecules were less than 20 nm apart and attributed to each event a nonzero pixel value, whose intensity is inversely related to the distance (Fig. 9; see Materials and methods). In our analysis, the pixel corresponding to a pLAT and pSLP76 protein pair at distances <20 nm depicts a signaling nanoterritory. In this case, nano defines the spacing between molecules at possible interacting distances (<20 nm) rather than the size of the domain.

Syt7 and MAL silencing reduced the frequency and extension of pLAT and pSLP76 signaling nanoterritories down to those of nonstimulated cells (αCD45; Fig. 9, A–I). Under stimulatory conditions, the majority of synaptic pLAT forms signaling nanoterritories with pSLP76 (Fig. 9, G and H). Signaling nanoterritories were present both at the fringes and, notably, within clusters, spanning ∼50% of pLAT cluster area (Fig. 9 I). Reinforcing the notion that vesicular LAT synaptic fusion promotes the formation of pLAT signaling hubs, signaling nanoterritories were present more extensively (∼75%) in elongated pLAT clusters (circularity <0.4) than in rounder ones (Fig. 9 J). Once more, provoking LAT vesicular fusion through thapsigargin treatment of MAL-silenced cells spread on αCD3-coated, but not on αCD45-coated, coverslips is sufficient to recover the frequency, extension, and morphology of signaling nanoterritories containing pLAT and pSLP76 to stimulatory levels (αCD3; Fig. 9, C–J and L–O).

These data indicate that there are two populations of functionally distinct pLAT clusters at the synapse: the preexisting round pLAT clusters, whose capacity for forming signaling nanoterritories with pSLP76 is low, and elongated pLAT clusters generated upon the synaptic fusion of vesicular LAT, which favors their molecular association with pSLP76 both at the rims and within pLAT clusters.

Lck-, TCRζ-, and LAT-regulated synaptic fusion is crucial for T cell activation leading to cytokine production

TCR-driven LAT phosphorylation leads to MAP kinase activation, CD69 up-regulation, and cytokine production (Acuto et al., 2008). To determine the contribution of regulated vesicular traffic to TCR-triggered T cell activation, we interrupted the Lck, TCRζ, and LAT vesicle traffic cascade by silencing either MAL or Syt7.

In primary CD4 T cells, activation events downstream of LAT, such as Erk1/2 activation, CD69 surface up-regulation, and IL-2 and IFN-γ cytokine production were all significantly inhibited in MAL- and Syt7-silenced cells (Fig. 10, A–G). Importantly, the increase in cytosolic calcium levels in MAL-silenced cells by thapsigargin or ionomycin restored an IL-2 and IFN-γ production comparable to control cells (Fig. 9, C–F, right). These results underscore the role of Lck-, TCRζ-, and LAT-regulated vesicle traffic in TCR signal integration conducive to T cell function.

DISCUSSION

It is increasingly clear that vesicle traffic achieves a variety of effects on signal transduction and, conversely, that receptor signaling regulates the exocytic machinery. Here, we sought to determine how the highly specific compartmentalization of Lck, LAT, and TCRζ contributes to the functional nanoscale organization of the immunological synapse and to its capacity to transduce downstream activation signals leading to cytokine production.

The molecular machinery that regulates the vesicular delivery of signaling molecules at the immunological synapse is largely unknown. We have analyzed this machinery by detailing its traffic regulators: Rab GTPases and SNARE proteins. We found that although Lck, LAT, and TCRζ traffic through exocytic compartments, there is no overlap in their traffic regulators (Fukuda, 2008). Lck localizes to the calcium-insensitive Rab11b/MAL compartment, whereas LAT and TCRζ traffic through a calcium-sensitive Rab27a-Rab37-Ti-VAMP and Rab3d-Rab8b-Ti-VAMP vesicular compartments, respectively. Interestingly, except for Rab8b, the exocytic traffic regulators present in Lck, LAT, or TCRζ vesicles have been also implicated in either cytokine secretion (Huse et al., 2006), or cytotoxic granules release (Ménager et al., 2007; Marcet-Palacios et al., 2008), at the CD4 and CD8 T cell synapses, respectively.

In cytotoxic T cell granule exocytosis (de Saint Basile et al., 2010) and in lymphocyte migration (Colvin et al., 2010), stimulus-induced vesicle fusion is regulated by synaptotagmins (Syt), which couple calcium influx to the formation of SNARE complexes. Previously, we have shown (Das et al., 2004) that syntaxin-4 and SNAP-23, two plasma membrane t-SNARE proteins, accumulate at the CD4 T cell–APC interface, which provides a molecular basis for selective vesicle fusion at the immunological synapse. However, SNARE complexes required for calcium-dependent exocytic vesicle fusion at the synapse

clusters per square micrometer is as follows: siCtr, $n = 24$; siSyt7, $n = 21$; siMAL, $n = 14$; siMAL TPS, $n = 11$; αCD45, $n = 20$; and αCD45 TPS, $n = 22$. (H) Number of clusters per square micrometer is as follows: siCtr, $n = 18$; siSyt7, $n = 21$; siMAL, $n = 14$; siMAL TPS, $n = 11$; αCD45, $n = 19$; and αCD45 TPS, $n = 22$. (I) Mean percentage per cell of the area occupied by signaling nanoterritories within each individual pLAT cluster $n \geq 11$ cells. (J–O) Percentage of the area occupied by signaling nanoterritories with respect to the total pLAT area (as in G) in function of cluster circularity value bracket for $n \geq 11$ cells. Images representative of three experiments. ***, $P \leq 0.0001$; **, $P \leq 0.01$; *, $P \leq 0.05$; Mann-Whitney test. Each circle represents a cell. Bar, 10 µm.

Published October 7, 2013

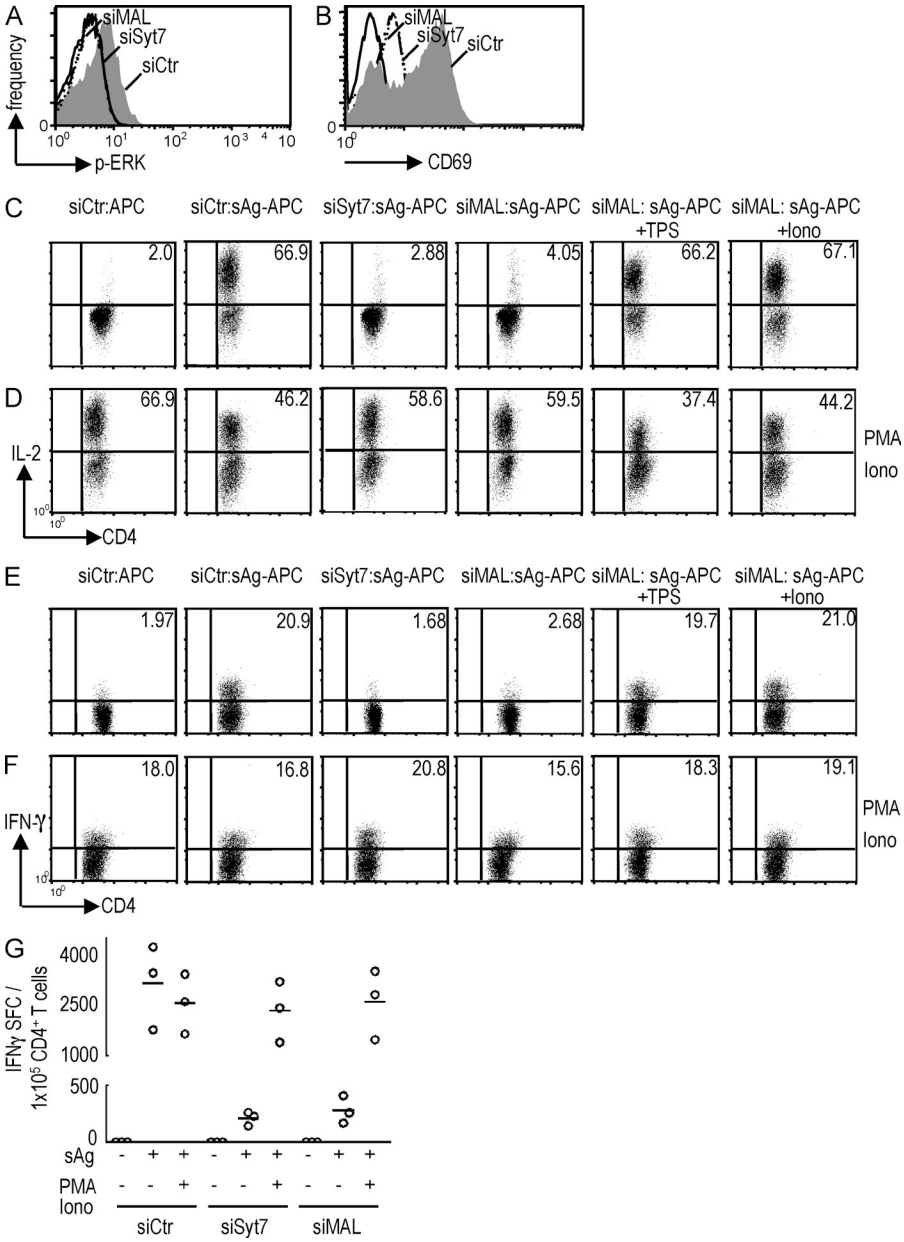

Figure 10. Syt7 or MAL silencing inhibit T cell activation. Primary CD4 T cells transfected with siRNA Syt7 (siSyt7), siRNA MAL (siMAL), or siRNA control (siCTR) were activated with superantigen-pulsed Raji cells for 10 min (A), 4 h (B), or 16 h (C–G). MAL-silenced cells were antigen-stimulated in the absence (siMAL) or in the presence of thapsigargin (siMAL TPS) or ionomycin (siMAL Iono). Calcium ionophore and phorbol myristate acetate (PMA-iono) were added as positive control (D, F, and G). Cells were analyzed by flow cytometry. (A) Erk activation by CD4 T cells determined by intracellular staining gated on $CD4^+$ cells. (B) Frequency of $CD69^+CD3^+$ T cells determined by surface staining. (C–F) IL-2 and IFN-γ production by CD4 T cells was determined by intracellular cytokine staining gated on $CD4^+$ cells. (G) Number of IFN-γ–secreting cells revealed by ELISPOT, each open circle represents an individual experiment. Images representative of three experiments.

were not identified. Here, we found that LAT and TCRζ vesicular compartments display Ti-VAMP/VAMP7. This v-SNARE mediates lysosomal exocytosis through the interaction with syntaxin-4 and SNAP-23, the two t-SNARES that cluster at the immunological synapse (Das et al., 2004), and with the vesicle fusion regulator Syt7 (Rao et al., 2004; Colvin et al., 2010). Similarly, we show that Syt7 regulates the calcium-induced exocytosis of the LAT and TCRζ vesicular compartments, in response to TCR triggering. In contrast, Lck synaptic recruitment is regulated by MAL and might be fulfilled by the Rab11b ability to traffic in response to activatory signals (Ménager et al., 2007; Sugawara et al., 2009). We found that Lck vesicular compartment is released faster than the ones of LAT and TCRζ in response αCD3 stimulation (unpublished data). In a concerted manner, Lck vesicular delivery to the immunological synapse might trigger local calcium fluxes, which in turn would induce TCRζ and LAT vesicle release. Therefore, Lck is the signal switch and calcium the mediator of a vesicular traffic and fusion amplification loop that delivers TCRζ and LAT, building up a fully competent signaling synapse.

Our results are consistent with the observation that Lck is constitutively active in resting CD4 T cells and its total activity is not increased upon TCR triggering (Nika et al., 2010). We propose that rather than controlling its phosphoactive status, TCR engagement triggers the delivery of vesicular Lck to the immunological synapse concentrating it locally and rapidly.

The relevance of LAT localization (plasma membrane versus vesicles) for TCR signal transduction is a subject of active debate. Previous studies (Purbhoo et al., 2010; Williamson et al.,

Published October 7, 2013

2011) put forward a role for LAT vesicles in TCR signaling, challenging previous studies that demonstrated the requirement of LAT plasma membrane oligomerization and cis phosphorylation (Houtman et al., 2006) for TCR signal transduction. Moreover, Larghi et al. (2013) very recently proposed that a VAMP7-mediated LAT vesicle docking to the synapse was responsible for TCR signaling. In contrast, another recent work (Balagopalan et al., 2013), using a CD4-LAT chimeric protein, proposed that it is mainly plasma membrane LAT that is phosphorylated and incorporated into microclusters, with minor influence from its vesicular pool. Although the phosphorylation of plasma membrane LAT appears clear, it is not clear whether CD4-LAT chimeras are properly targeted to stimulus-regulated exocytic compartments. Therefore, the mechanistic aspects of this process (plasma membrane, versus vesicle transient approach, docking, or fusion), its regulation and the relative relevance of both LAT origins for TCR signaling remain ill defined.

By combining molecular control over TCRζ and LAT vesicle fusion with dual-color dSTORM and TIRF microscopy approaches, we unveil here that the nanoscale organization of pLAT and pSLP76 upon TCR stimulation depends on TCRζ and LAT vesicle fusion at the synaptic membrane. In contrast, pTCRζ and pZAP70 nanocluster organization was only mildly affected by these fusion events. To our knowledge, this is the first observation in which the fusion of vesicles carrying signaling molecule impacts the functional nanoscale organization of the immunological synapse. First, inhibition of TCRζ and LAT vesicular fusion resulted in a pLAT and pSLP76 patterns similar to nonstimulated cells, suggesting that plasma membrane resident pLAT contributes poorly to early TCR signaling. Second, the fusion of vesicular LAT is accountable for the pLAT clusters increase in size, number, and density. Third, LAT compartment fusion originates a subpopulation of elongated clusters that act as signaling hubs through extensive formation of signaling nanoterritories with pSLP76. Fourth, the activatory synapse nanoscale organization was rescued when LAT vesicular retention due to MAL silencing was bypassed by thapsigargin, which causes a calcium flux that mediates LAT and TCRζ synaptic fusion. Finally, TCR stimulation was needed for thapsigargin-induced synapse nanoscale organization, as it did not occur in αCD45-plated cells.

We detected a wide range of clustering, from a few detections to larger spatial domains, as described previously (Lillemeier et al., 2010; Sengupta et al., 2011; Williamson et al., 2011). The elongated pLAT clusters, observed upon vesicular LAT fusion at the synapse, are consistent with high resolution imaging studies that described that LAT signaling clusters may represent discrete interdigitating domains in T cells (Douglass and Vale, 2005; Lillemeier et al., 2006) and compatible with plasma membrane confinement zones (Kusumi et al., 2010). Super-resolution imaging has not been able to resolve the pLAT cluster size obtained by different studies with Sherman et al. (2011) reporting a predominance of very small LAT clusters. This apparent discrepancy might result from the terminology used and/or the different statistical methods applied to segment clusters. The inability of other studies (Purbhoo et al., 2010; Williamson et al., 2011) to detect elongated pLAT clusters at later time-points (10 min) might be caused by the endocytosis of LAT clusters, which could also explain the presence of the late endocytic marker Rab7 in LAT vesicles (Purbhoo et al., 2010).

The fact that elongated pLAT clusters preferentially recruit pSLP76 indicates that they are especially adept at conveying TCR signaling, when compared with isolated molecules or to clusters formed by 3–4 LAT molecules. This may occur by various means: (1) elongated clusters may offer a higher contact area for a given cluster volume; (2) they may increase the duration and affinity of interaction allowing for the slow phosphorylation reactions to occur; (3) they may favor the assembly of different signaling pathways. Accordingly, we found that single pLAT and pSLP76 molecules associate in signaling nanoterritories both at the fringes and within clusters. This discrete molecular association of pLAT and pSLP76 within clusters has not been previously appreciated (Lillemeier et al., 2010; Sherman et al., 2011) and might result from hop diffusion. Our data are compatible with a model whereby specialized intracellular calcium microdomains (Wei et al., 2009) and the presence of SNAREs in particular plasma membrane subdomains would locally target LAT vesicle fusion (Video 1). Within those subdomains, delivered LAT would rapidly cluster, as a direct consequence of LAT oligomerization (Houtman et al., 2006). It remains to be addressed whether elongated pLAT clusters originate directly from vesicular LAT, or if they originate because of lateral movement of the plasma membrane after vesicle fusion. The rounder clusters observed in the absence of LAT vesicle fusion may represent more static plasma membrane–resident nanostructures with other possible functions. Novel approaches combining super-resolution microscopy with live cell imaging will help test this proposition.

Finally, MAL or Syt7 silencing blocked TCR signal integration through the inhibition of Erk activation, CD69 up-regulation and IL-2 and IFN-γ production. The extensive restoration of IL-2 and IFN-γ release induced by thapsigargin or ionomycin treatment in MAL-silenced cells, or by PMA-ionomycin in Syt7-silenced cells, shows that neither MAL nor Syt7 silencing affected cytokine secretion. Thus, we conclude that TCRζ- and LAT-regulated fusion at the synapse determine the signaling nanoterritories required for TCR signal amplification and T cell effector function.

In conclusion, this work shows that the spatiotemporal regulation of TCR signaling results from the regulated fusion of vesicles carrying signaling molecules. TCR signaling is not merely a function of which signaling molecules are present at the synaptic membrane but also a function of their subcellular origin and traffic regulation.

MATERIALS AND METHODS

Cell cultures and transfections. Jurkat cells clone J77cl20 and the APC Raji B cells were grown in complete RPMI medium containing 10% (vol/vol) fetal bovine serum, nonessential amino acids, and L-glutamine (Das et al., 2004). DNA constructs were inserted into Jurkat cells using the Invitrogen Neon Transfection system. Transiently transfected cells were imaged 24–48 h after transfection. Transfection efficiency was evaluated by flow cytometry.

Published October 7, 2013

Primary CD4 T cell culture and transfections. Peripheral blood cells were grown in the presence of staphylococcal enterotoxin B (SEB; 5 ng/ml) and TSST-1 (5 ng/ml) for 48– 72 h, washed, and cultured in IL-2–containing medium (20–50 U/ml) for 7 d, at which time they were restimulated with SEB (5 ng/ml), TSST-1 (5 ng/ml), and PHA (0.4 µg/ml) for 24 h. Cells were resuspended for another 24 h in IL-2–containing medium, and then negatively selected through magnetic bead purification (MACS; Miltenyi Biotec) according to the manufacturer's instructions. CD4 T cells were cultured for 5–6 d in complete RPMI medium enriched with 20 U/ml of human IL-2. DNA constructs were electroporated into primary CD4 T cells using the Invitrogen Neon Transfection system (PBMC program). Primary CD4 T cells were imaged 24–48 h after electroporation. Transfection efficiency was evaluated by flow cytometry.

Cell stimulation for confocal microscopy. Immunological synapses formation were promoted by incubating Raji cells unpulsed or pulsed with superantigen (10 µg/ml, 20 min), either SEE for Jurkat or SEB+TSST1 for primary CD4 T cells at a 1:1 T cell/APC ratio for 30 min.

Confocal imaging. Cells plated onto poly-L-lysine–coated coverslips were fixed in 4% paraformaldehyde for 15 min, rinsed, and treated with 50 mM NH_4Cl in PBS for 10 min to quench the aldehyde groups. After PBS wash, nonspecific binding was prevented by 15-min incubation with 1% BSA (wt/vol) and 0.05% saponin in PBS, used throughout the procedure as staining and washing buffer. After 1-h incubation with the indicated primary antibodies, cells were rinsed and incubated with the corresponding secondary antibodies. The anti-Lck mAb (3A5) and the anti-TCRζ mAb were obtained from Santa Cruz Biotechnology, Inc.; the anti-LAT polyclonal antibody was purchased from EMD Millipore; the anti-pY^{142}TCRζ mAb was purchased from BD; the anti-pY^{191}LAT polyclonal antibody was obtained from BioSource, the anti-pY^{394}Src polyclonal antibody was from MBL. The cyanine 3 (Cy3)-coupled anti–mouse IgG2b, the fluorescein-coupled anti–mouse IgG2b, the fluorescein-coupled anti–mouse IgG2a and the fluorescein-coupled goat anti–rabbit Ig were from Jackson ImmunoResearch Laboratories. Alexa Fluor 488–coupled goat antifluorescein antibody was obtained from Molecular Probes. Cell grade thapsigargin was purchased from Sigma-Aldrich. Confocal images were obtained using a LSM 700 confocal microscope (Carl Zeiss) over a 63× objective. Z stack optical sections were acquired at 0.2 µm depth increments, and both green and red laser excitation were intercalated to minimize cross-talk between the acquired fluorescence channels.

Confocal image post-treatment. Complete image stack deconvolution was performed with Huygens Essential (version 3.0, Scientific Volume Imaging), and 2D images were generated from a maximum intensity projection over a 3D volume cut of 1 µm depth, centered either on the vesicular compartment when visible or on the cell center.

Quantification of Lck, LAT, and TCRζ subcellular distribution. The plasma membrane of CD4 T cells was surface labeled with anti-CD2 mAbs (clone TS2/18; American Type Culture Collection [ATCC]). Vesicular compartments were intracellularly stained for the proteins of interest. Confocal images were acquired at 2-µm increments in the z-axis. Two to three contiguous optical sections contained the whole-cell fluorescence information. Plasma membrane segmentation was implemented through the Weka supervised machine-learning segmentation algorithm (Frank et al., 2004), using the Fiji image analysis software (Schindelin et al., 2012). To teach the machine-learning algorithm, we have manually segmented at least three datasets for each imaging condition. 2D probability maps generated by the Weka algorithm were then converted into binary masks and used to delimitate the internal and external outlines of the plasma membrane. Our automated method provides accurate segmentation of the plasma membrane in the stained tracts and reconstructs the approximate location of the unstained tracts resulting from plasma membrane labeling gaps. % vesicular compartment FI = Total Fl − Plasma membrane Fl/Total Fl × 100.

Manipulation of intracellular calcium levels. Jurkat and primary CD4 T cells were treated with medium alone or medium containing either 5 µM of the endoplasmic reticulum calcium ATPase inhibitor thapsigargin or 5 µM of the calcium ionophore ionomycin for 30 min, washed, and processed for microscopy.

siRNA-silencing experiments and Western blot analysis. Jurkat or primary CD4 T cells were transfected once with siRNA oligonucleotide pools (Invitrogen) targeting either Syt7, MAL, or with a nontargeting siRNA pool, as negative control (siCtr; Thermo Fisher Scientific). Shutdown efficiency was assessed 72 h after transfection. Cellular extracts were prepared with lysis buffer (containing β-mercaptoethanol) and complete protease inhibitors (Roche). After separation by PAGE, proteins were transferred to nitrocellulose membranes. Anti-Syt7 antibody (rabbit polyclonal; Sigma-Aldrich) was added at 1:200 dilution, whereas anti-MAL antibody (provided by M.A. Alonso) was added at 1:200 dilution in a solution of 1% (wt/vol) dehydrated milk in Tris HCl-buffered saline with 0.05% (vol/vol) Tween-20. Analysis of β-actin served as a loading control; anti–β-actin was added to the blots at a dilution of 1:100,000 in a solution of 1% (wt/vol) dehydrated milk in Tris HCl-buffered saline with 0.05% (vol/vol) Tween-20. Blots were developed with ECL Plus reagents (GE Healthcare).

dSTORM sample preparation. Glass coverslips were washed 2–3 times in optical grade acetone and soaked overnight in 0.1 M KOH. Coverslips were then thoroughly rinsed in deionized water and dried. The glass coverslips were coated overnight at room temperature with 0.001% poly-L-Lysine (Sigma-Aldrich) diluted in PBS. Dried coverslips were subsequently incubated with stimulatory (αCD3 mAb MEM 92; EXBIO) or nonstimulatory (αCD45 mAb GAP 8.3; ATCC) antibodies at concentration of 10 µg/ml overnight at 4°C. Cells were resuspended in imaging buffer (Heilemann et al., 2008), and 500,000 cells were dropped onto the coverslips and incubated for 3 min at 37°C. In some cases thapsigargin (5 µM) was added during the incubation period. Cells were then fixed with 4% paraformaldehyde for 30 min at room temperature. After 15-min incubation with blocking buffer, fixed cells were incubated for 1 h with primary antibodies. The anti-pY^{191}LAT polyclonal antibody was obtained from BioSource; the anti-pY^{118}SLP-76 was purchased from BD and the anti-pY^{319}ZAP-70 was obtained from Cell Signaling Technology. Cells were washed and incubated for 45 min, with secondary antibodies conjugated to Alexa Fluor 568 or to Cy5 (Molecular Probes). To maximize the number of detected molecules, care was taken to minimize photobleaching: cells were embedded in oxygen scavenger buffer as previously described (Heilemann et al., 2008), imaged on the same day of labeling, and kept in the dark until imaged. Tetraspeck beads (100 nm diameter; Invitrogen) were mounted with the sample as fiduciary landmarks and later tracked for computational drift correction and chromatic realignment.

Widefield and dSTORM acquisition procedure. For each coverslip, 8–10 area fields (55 × 55 μm^2 per field, 107 × 107 nm^2 per pixel) were preselected on the microscope for imaging; each field typically contained between 1 and 6 cells. We developed the automated acquisition sequence based on the open-source µManager microscopy acquisition software (Edelstein et al., 2010). First, the field-of-view was centered in the preselected coverslip region. The cells were then imaged by triple-color epifluorescence (GFP, Alexa Fluor 568, and Cy5). The z-stack acquisition was performed at 200 nm z-steps encompassing the size of the Jurkat cell. This enabled to determine the proper localization and expression levels of the proteins of interest in the analyzed cells. XZ and YZ wide-field projections were taken to monitor LAT vesicular compartment delivery at the synapse. Finally, the objective was refocused on the surface of the coverslip, TIRF illumination was switched on into and a dSTORM image-stream acquisition was performed for the Cy5 channel (635 nm laser-excitation at 1.7 kW/cm^2, 662–690 nm emission) and then the Alexa Fluor 568 channel (561 nm laser-excitation at 2.4 kW/cm^2, 589–625 nm emission), each composed of 20.000 images acquired at 30 Hz. Imaging parameters were set using the µManager freeware running on a desktop PC. Laser control was achieved with custom software

Published October 7, 2013

(Henriques et al., 2010). A detailed description of the imaging apparatus can be found in (Henriques et al., 2010). Custom algorithms were applied to determine the position map of the identified molecules, as well as their distance from each other, as described in the next section.

Single-molecule detection and localization. Particle detection and localization was carried by a custom algorithm using the Fiji-Jython scripting interface (Schindelin et al., 2012). The algorithm uses remote procedure calls to connect to a Python virtual machine implementing the DAOSTORM algorithm (Holden et al., 2011). This method uses DAOSTORM to detect and localize particles in both unprocessed and treated frames combining time averaging with frame subtraction in a process similar to a gSHRImP analysis (Simonson et al., 2011). Multiple detections caused by the same particle appearing in adjacent frames (distances smaller than 0.25 pixels) are merged and detections with low fitting accuracy are discarded. For our acquisition settings we have observed that combining the DAOSTORM engine with gSHRImP analysis allows us to decrease the localization error by up to 20% when compared with simple DAOSTORM analysis while supporting up to a threefold increase in particle detection.

Super-resolution drift correction and chromatic realignment. Before particle detection and localization, fiduciary beads were identified and marked, typically more than five. Sample drift was then calculated by tracking the group displacement of selected beads throughout the acquired image sequence. After particle detection and localization, the position of each particle was readjusted by subtracting the drift identified at the corresponding time-point. Chromatic realignment was generated after drift correction, the channel displacement of beads was calculated, a position correction for each particle on the Cy5 channel was then computed and applied by subtracting the average channel-displacement of the closest beads, weighted by their distance to the particle. To estimate the chromatic realignment error, beads were randomly selected and the corresponding chromatic realignment vector was calculated not using their channel displacement information, an ~3 nm error was observed by comparing the chromatic realignment vector and channel-displacement vector.

Super-resolution estimation and image reconstruction. The localization error was calculated by measuring the full-width-half-maximum of manually selected small detection clusters (5–21 particles per cluster; Bates et al., 2007). The average localization error for Alexa Fluor 568 was 19 nm (7 clusters) and Cy5 was 16 nm (6 clusters). Final super-resolution reconstructions were then generated in Fiji (Schindelin et al., 2012) by creating images with 10-nm pixel-size and additively superimposing a Gaussian kernel of 20-nm full-width-half-maximum to each particle.

Super-resolution protein cluster segmentation and characterization. Protein cluster segmentation was performed through the automatic triangle threshold implementation of the Fiji software (Schindelin et al., 2012). The triangle threshold method was applied individually to regions-of-interest demarking a single-cell, allowing us to discriminate clustered particle detections at the immunological synapse. Background detections (false-detection) caused by noise fluctuations or motile unbound labeled antibodies were minimally present in the thresholded images. For each segmented particle cluster in the rendered image, the following properties were measured: particles density, area, circularity, and diameter. We verified that cell illumination was considerably homogenous for the individual cell regions-of-interest, but slightly nonhomogeneous for the full field-of-view due to the Gaussian profile of the laser illumination in our microscopy setup. Additionally, we quantified the percentage of overlap between the segmented clusters and corresponding interdistance maps (see below).

Interdistance maps calculation. Interdistance maps are artificially generated super-resolution images where pixel values identify the presence of a pair of pLAT and pSLP76 proteins at distances <20 nm away from each other (detailed below). These maps are insensitive to particle concentration. The presence of either a single or more pairs in a region of space represented by a pixel will lead to a pixel value equal to the shortest distance between any of the pairs. This feature allowed us to map and easily visualize regions of space where proteins are closely packed or potentially interact, but not necessarily in large numbers. Concentration insensitivity has the potential to augment false detections. To minimize any unwanted false contributions, we created a prefiltering process described below that severely diminishes the presence of erroneous detections.

Pre-filtering. Throughout dSTORM image acquisition, an individual fluorophore typically undergoes multiple cycles of photoswitching, leading to several detections of the same fluorophore in a region whose extent is determined by the localization accuracy (Heilemann et al., 2008). We have verified that for both Alexa Fluor 568 and Cy5 imaging conditions, small detection clusters featured 5 or more particles typically generated by individual fluorophore photoswitching. Based on this feature, we constructed a prefiltering algorithm that eliminates any detected particle that does not have at least 5 neighboring particles of the same color at distances smaller than 10 nm. We verified that these threshold values reduced spatially random false detections within the cells while severely removing detections outside and keeping the morphology of the labeled ultrastructures.

Interdistance map generation. For a specific cell, the interdistance map is generated by creating an image with the same pixel size (10 nm) and image size as the corresponding super-resolution reconstructions. Detected particles for the Cy5 and Alexa568 channels are prefiltered as described above. Subsequently, for each particle identified in the Cy5 channel the closest particle in the Alexa568 channel is searched for. For each found pair, if the Euclidian distance between both particles is smaller than 20 nm and there is no other pair of particles with a smaller distance within the same pixel region of space, then the corresponding pixel value is set to be equal to the pair distance, or a null value otherwise. For convenience, we then apply an inverted grayscale lookup table to the image, giving pixels a bright value where pairs are found at very close distances, dim value for short distances and black value where no pairs have been found at distances smaller than 20 nm.

Flow cytometry. Primary CD4 T cells were knocked down for either Syt7 or MAL expression 3 d before the experiment using siRNA oligonucleotides or scramble oligo as control, as described above. For Lck, LAT, TCRζ, SLP76, and ZAP70 phosphorylation analysis, 5×10^5 CD4 T cells were co-cultured at 1:1 ratio with Raji cells for 30 min in the presence or absence of SEE (10 μg/ml). Thapsigargin (5 μM) was added to some of the samples. The cells were fixed and permeabilized (Cytofix/Cytoperm Plus; BD) and stained with the antibodies of interest at room temperature. For Erk phosphorylation analysis, 5×10^5 primary CD4 T cells prepared as described above were co-cultured at 1:1 ratio with Raji cells for 10 min in the presence or absence of SEB and TSST1 superantigens (10 μg/ml), and then fixed with 4% paraformaldehyde and permeabilized with saponin. For CD69 up-regulation analysis, 5×10^5 cells primary CD4 T cells prepared as described above were co-cultured at 1:1 ratio with Raji cells in the presence or absence of SEB and TSST1 for 4 h. For cytokine production analysis, 10^{10} cells primary CD4 T cells prepared as described above were stimulated with either Raji cells loaded with SEB and TSST1 (10 μg/ml) or medium at 1:10 ratio for 16 h. Thapsigargin (5 μM), ionomycin (500 ng/ml), or PMA (20 ng/ml) plus ionomycin (500 ng/ml) were added to some of the samples. Brefeldin A (2 mg/ml; Sigma-Aldrich) was added for the last 15 h. Cells were washed and stained with FITC anti-CD4 (RPA-T4; BD) for 20 min at 4°C. The cells were permeabilized (Cytofix/Cytoperm Plus; BD) and stained with PE anti–IFN-γ (4S.B3; BD) and APC anti–IL-2 (MQ1-17H12; BD) at room temperature. Erk, CD69 up-regulation, and IL-2/IFN-γ production were determined gating on primary CD4 T cells. We used a FACSORT with data analysis in FlowJo (Tree Star).

Single-cell ELISPOT assay for IFN-g-secreting cells. Primary CD4 T cells were electroporated with siRNA oligonucleotides for Syt7, MAL, or scramble control 3 d before the experiment, as described above. 96-well

filtration plates (Millipore) were coated with anti–human IFN-γ antibody (1-DIK; Mabtek). 2×10^5 cells primary CD4 T cells prepared as described above were plated per well and stimulated with either Raji cells loaded with SEB or medium at 1:10 ratio, or PMA (20 ng/ml) and ionomycin (500 ng/ml) for 16 h. After culture, the plates were washed, followed by incubation with biotinylated anti–IFN-γ antibody (7B6-1; Mabtek). Spots were developed using freshly prepared substrate buffer (0.3 mg/ml of 3-amino-9-ethyl-carbazole and 0.015% H_20_2 in 0.1 M sodium acetate, pH 5.0). The frequency of IFN-γ–secreting CD4 T cells was calculated based on the percentage of CD4 T cells present in the well.

3D time-lapse microscopy. GFP epifluorescence imaging was performed by continuous acquisition of sequences of z-stacks with 0.5-µm z-steps, 7–20-µm z-range, for 3–10 min. These values were selected to optimize the visualization of the cell adherence to the coverslip and formation of the immune synapse, and to capture a sufficient cell volume and minimize photodamage. While imaging, cells were kept at 37°C in an incubator encompassing most of the microscope body. For simplicity of visualization, time-lapse movies were generated in Fiji (Schindelin et al., 2012) by creating a horizontal montage where each lateral element corresponds to a maximum intensity projection over a 2.5-µm z-range. Before creation of the time-lapse movies, datasets were denoised by a 3D Gaussian blur of 0.5 × 0.5 × 0.5 pixels (x sigma, y sigma, z sigma).

Statistical analysis. Were performed by Mann–Whitney nonparametric test using Prism software (GraphPad).

Online supplemental material. Video 1 shows LAT-GFP expressing cells deposited on an αCD3 stimulatory surface. Online supplemental material is available at http://www.jem.org/cgi/content/full/jem.20130150/DC1.

We are thankful for the technical assistance of Imagopole, C. Cuche, and M. Lelek. We thank A. Echard, J. Enninga, T. Galli, and B Goud for reagents and O. Schwartz for critical reading of the manuscript.

This work was funded by grants from Agence National de Recherche sur le SIDA (ANRS), Agence National de Recherche (ANR-07-MIME-030; ANR-2011-Blanc-SVSE3-025), Institut Pasteur PTR-214, Ile de France DIM-MALINF (to A. Alcover, M.-I. Thoulouze, and C. Zimer) and BFU2009-07886 and CSD2009-00016 from the Spanish Ministry of Science and Innovation (to M.A. Alonso). H. Soares was funded by the Institut Pasteur PTR-214, EMBO long-term fellowship, ANR, Sidaction, and ANRS. R. Henriques was funded by an Institut Pasteur-Roux fellowship.

The authors declare to have no financial conflict of interest.

Submitted: 21 January 2013
Accepted: 28 August 2013

REFERENCES

Acuto, O., V. Di Bartolo, and F. Michel. 2008. Tailoring T-cell receptor signals by proximal negative feedback mechanisms. *Nat. Rev. Immunol.* 8:699–712. http://dx.doi.org/10.1038/nri2397

Alcover, A., and M.I. Thoulouze. 2010. Vesicle traffic to the immunological synapse: a multifunctional process targeted by lymphotropic viruses. *Curr. Top. Microbiol. Immunol.* 340:191–207. http://dx.doi.org/10.1007/978-3-642-03858-7_10

Antón, O., A. Batista, J. Millán, L. Andrés-Delgado, R. Puertollano, I. Correas, and M.A. Alonso. 2008. An essential role for the MAL protein in targeting Lck to the plasma membrane of human T lymphocytes. *J. Exp. Med.* 205:3201–3213. http://dx.doi.org/10.1084/jem.20080552

Balagopalan, L., V.A. Barr, R.L. Kortum, A.K. Park, and L.E. Samelson. 2013. Cutting edge: cell surface linker for activation of T cells is recruited to microclusters and is active in signaling. *J. Immunol.* 190:3849–3853. http://dx.doi.org/10.4049/jimmunol.1202760

Bates, M., B. Huang, G.T. Dempsey, and X. Zhuang. 2007. Multicolor super-resolution imaging with photo-switchable fluorescent probes. *Science.* 317:1749–1753. http://dx.doi.org/10.1126/science.1146598

Bonello, G., N. Blanchard, M.C. Montoya, E. Aguado, C. Langlet, H.T. He, S. Nunez-Cruz, M. Malissen, F. Sanchez-Madrid, D. Olive, et al. 2004. Dynamic recruitment of the adaptor protein LAT: LAT exists in two distinct intracellular pools and controls its own recruitment. *J. Cell Sci.* 117:1009–1016. http://dx.doi.org/10.1242/jcs.00968

Chaineau, M., L. Danglot, and T. Galli. 2009. Multiple roles of the vesicular-SNARE TI-VAMP in post-Golgi and endosomal trafficking. *FEBS Lett.* 583:3817–3826. http://dx.doi.org/10.1016/j.febslet.2009.10.026

Colvin, R.A., T.K. Means, T.J. Diefenbach, L.F. Moita, R.P. Friday, S. Sever, G.S. Campanella, T. Abrazinski, L.A. Manice, C. Moita, et al. 2010. Synaptotagmin-mediated vesicle fusion regulates cell migration. *Nat. Immunol.* 11:495–502. http://dx.doi.org/10.1038/ni.1878

Das, V., B. Nal, A. Dujeancourt, M.I. Thoulouze, T. Galli, P. Roux, A. Dautry-Varsat, and A. Alcover. 2004. Activation-induced polarized recycling targets T cell antigen receptors to the immunological synapse; involvement of SNARE complexes. *Immunity.* 20:577–588. http://dx.doi.org/10.1016/S1074-7613(04)00106-2

de Saint Basile, G., G. Ménasché, and A. Fischer. 2010. Molecular mechanisms of biogenesis and exocytosis of cytotoxic granules. *Nat. Rev. Immunol.* 10:568–579. http://dx.doi.org/10.1038/nri2803

Douglass, A.D., and R.D. Vale. 2005. Single-molecule microscopy reveals plasma membrane microdomains created by protein-protein networks that exclude or trap signaling molecules in T cells. *Cell.* 121:937–950. http://dx.doi.org/10.1016/j.cell.2005.04.009

Dustin, M.L., and D. Depoil. 2011. New insights into the T cell synapse from single molecule techniques. *Nat. Rev. Immunol.* 11:672–684. http://dx.doi.org/10.1038/nri3066

Edelstein, A., N. Amodaj, K. Hoover, R. Vale, and N. Stuurman. 2010. Computer control of microscopes using microManager. *Curr Protoc Mol Biol* Chapter 14:Unit14 20.

Ehrlich, L.I.R., P.J.R. Ebert, M.F. Krummel, A. Weiss, and M.M. Davis. 2002. Dynamics of p56lck translocation to the T cell immunological synapse following agonist and antagonist stimulation. *Immunity.* 17:809–822. http://dx.doi.org/10.1016/S1074-7613(02)00481-8

Finetti, F., S.R. Paccani, M.G. Riparbelli, E. Giacomello, G. Perinetti, G.J. Pazour, J.L. Rosenbaum, and C.T. Baldari. 2009. Intraflagellar transport is required for polarized recycling of the TCR/CD3 complex to the immune synapse. *Nat. Cell Biol.* 11:1332–1339. http://dx.doi.org/10.1038/ncb1977

Frank, E., M. Hall, L. Trigg, G. Holmes, and I.H. Witten. 2004. Data mining in bioinformatics using Weka. *Bioinformatics.* 20:2479–2481. http://dx.doi.org/10.1093/bioinformatics/bth261

Fukuda, M. 2008. Regulation of secretory vesicle traffic by Rab small GTPases. *Cell. Mol. Life Sci.* 65:2801–2813. http://dx.doi.org/10.1007/s00018-008-8351-4

Heilemann, M., S. van de Linde, M. Schüttpelz, R. Kasper, B. Seefeldt, A. Mukherjee, P. Tinnefeld, and M. Sauer. 2008. Subdiffraction-resolution fluorescence imaging with conventional fluorescent probes. *Angew. Chem. Int. Ed. Engl.* 47:6172–6176. http://dx.doi.org/10.1002/anie.200802376

Henriques, R., M. Lelek, E.F. Fornasiero, F. Valtorta, C. Zimmer, and M.M. Mhlanga. 2010. QuickPALM: 3D real-time photoactivation nanoscopy image processing in ImageJ. *Nat. Methods.* 7:339–340. http://dx.doi.org/10.1038/nmeth0510-339

Holden, S.J., S. Uphoff, and A.N. Kapanidis. 2011. DAOSTORM: an algorithm for high- density super-resolution microscopy. *Nat. Methods.* 8:279–280. http://dx.doi.org/10.1038/nmeth0411-279

Houtman, J.C., H. Yamaguchi, M. Barda-Saad, A. Braiman, B. Bowden, E. Appella, P. Schuck, and L.E. Samelson. 2006. Oligomerization of signaling complexes by the multipoint binding of GRB2 to both LAT and SOS1. *Nat. Struct. Mol. Biol.* 13:798–805. http://dx.doi.org/10.1038/nsmb1133

Huse, M., B.F. Lillemeier, M.S. Kuhns, D.S. Chen, and M.M. Davis. 2006. T cells use two directionally distinct pathways for cytokine secretion. *Nat. Immunol.* 7:247–255. http://dx.doi.org/10.1038/ni1304

Kusumi, A., Y.M. Shirai, I. Koyama-Honda, K.G. Suzuki, and T.K. Fujiwara. 2010. Hierarchical organization of the plasma membrane: investigations by single-molecule tracking vs. fluorescence correlation spectroscopy. *FEBS Lett.* 584:1814–1823. http://dx.doi.org/10.1016/j.febslet.2010.02.047

Larghi, P., D.J. Williamson, J.M. Carpier, S. Dogniaux, K. Chemin, A. Bohineust, L. Danglot, K. Gaus, T. Galli, and C. Hivroz. 2013. VAMP7

controls T cell activation by regulating the recruitment and phosphorylation of vesicular Lat at TCR-activation sites. *Nat. Immunol.* 14:723–731. http://dx.doi.org/10.1038/ni.2609

Lasserre, R., and A. Alcover. 2010. Cytoskeletal cross-talk in the control of T cell antigen receptor signaling. *FEBS Lett.* 584:4845–4850. http://dx.doi.org/10.1016/j.febslet.2010.09.001

Lillemeier, B.F., J.R. Pfeiffer, Z. Surviladze, B.S. Wilson, and M.M. Davis. 2006. Plasma membrane-associated proteins are clustered into islands attached to the cytoskeleton. *Proc. Natl. Acad. Sci. USA.* 103:18992–18997. http://dx.doi.org/10.1073/pnas.0609009103

Lillemeier, B.F., M.A. Mörtelmaier, M.B. Forstner, J.B. Huppa, J.T. Groves, and M.M. Davis. 2010. TCR and Lat are expressed on separate protein islands on T cell membranes and concatenate during activation. *Nat. Immunol.* 11:90–96. http://dx.doi.org/10.1038/ni.1832

Marcet-Palacios, M., S.O. Odemuyiwa, J.J. Coughlin, D. Garofoli, C. Ewen, C.E. Davidson, M. Ghaffari, K.P. Kane, P. Lacy, M.R. Logan, et al. 2008. Vesicle-associated membrane protein 7 (VAMP-7) is essential for target cell killing in a natural killer cell line. *Biochem. Biophys. Res. Commun.* 366:617–623. http://dx.doi.org/10.1016/j.bbrc.2007.11.079

Ménager, M.M., G. Ménasché, M. Romao, P. Knapnougel, C.H. Ho, M. Garfa, G. Raposo, J. Feldmann, A. Fischer, and G. de Saint Basile. 2007. Secretory cytotoxic granule maturation and exocytosis require the effector protein hMunc13-4. *Nat. Immunol.* 8:257–267. http://dx.doi.org/10.1038/ni1431

Nika, K., C. Soldani, M. Salek, W. Paster, A. Gray, R. Etzensperger, L. Fugger, P. Polzella, V. Cerundolo, O. Dushek, et al. 2010. Constitutively active Lck kinase in T cells drives antigen receptor signal transduction. *Immunity.* 32:766–777. http://dx.doi.org/10.1016/j.immuni.2010.05.011

Pang, Z.P., and T.C. Südhof. 2010. Cell biology of Ca2+-triggered exocytosis. *Curr. Opin. Cell Biol.* 22:496–505. http://dx.doi.org/10.1016/j.ceb.2010.05.001

Purbhoo, M.A., H. Liu, S. Oddos, D.M. Owen, M.A. Neil, S.V. Pageon, P.M. French, C.E. Rudd, and D.M. Davis. 2010. Dynamics of subsynaptic vesicles and surface microclusters at the immunological synapse. *Sci. Signal.* 3:ra36. http://dx.doi.org/10.1126/scisignal.2000645

Rao, S.K., C. Huynh, V. Proux-Gillardeaux, T. Galli, and N.W. Andrews. 2004. Identification of SNAREs involved in synaptotagmin VII-regulated lysosomal exocytosis. *J. Biol. Chem.* 279:20471–20479. http://dx.doi.org/10.1074/jbc.M400798200

Schindelin, J., I. Arganda-Carreras, E. Frise, V. Kaynig, M. Longair, T. Pietzsch, S. Preibisch, C. Rueden, S. Saalfeld, B. Schmid, et al. 2012. Fiji: an open-source platform for biological-image analysis. *Nat. Methods.* 9:676–682. http://dx.doi.org/10.1038/nmeth.2019

Sengupta, P., T. Jovanovic-Talisman, D. Skoko, M. Renz, S.L. Veatch, and J. Lippincott-Schwartz. 2011. Probing protein heterogeneity in the plasma membrane using PALM and pair correlation analysis. *Nat. Methods.* 8:969–975. http://dx.doi.org/10.1038/nmeth.1704

Sherman, E., V. Barr, S. Manley, G. Patterson, L. Balagopalan, I. Akpan, C.K. Regan, R.K. Merrill, C.L. Sommers, J. Lippincott-Schwartz, and L.E. Samelson. 2011. Functional nanoscale organization of signaling molecules downstream of the T cell antigen receptor. *Immunity.* 35:705–720. http://dx.doi.org/10.1016/j.immuni.2011.10.004

Simonson, P.D., E. Rothenberg, and P.R. Selvin. 2011. Single-molecule-based super-resolution images in the presence of multiple fluorophores. *Nano Lett.* 11:5090–5096. http://dx.doi.org/10.1021/nl203560r

Stinchcombe, J.C., D.C. Barral, E.H. Mules, S. Booth, A.N. Hume, L.M. Machesky, M.C. Seabra, and G.M. Griffiths. 2001. Rab27a is required for regulated secretion in cytotoxic T lymphocytes. *J. Cell Biol.* 152:825–834. http://dx.doi.org/10.1083/jcb.152.4.825

Stojilkovic, S.S. 2005. Ca2+-regulated exocytosis and SNARE function. *Trends Endocrinol. Metab.* 16:81–83. http://dx.doi.org/10.1016/j.tem.2005.02.002

Sugawara, K., T. Shibasaki, A. Mizoguchi, T. Saito, and S. Seino. 2009. Rab11 and its effector Rip11 participate in regulation of insulin granule exocytosis. *Genes Cells.* 14:445–456. http://dx.doi.org/10.1111/j.1365-2443.2009.01285.x

Wei, C., X. Wang, M. Chen, K. Ouyang, L.S. Song, and H. Cheng. 2009. Calcium flickers steer cell migration. *Nature.* 457:901–905. http://dx.doi.org/10.1038/nature07577

Williamson, D.J., D.M. Owen, J. Rossy, A. Magenau, M. Wehrmann, J.J. Gooding, and K. Gaus. 2011. Pre-existing clusters of the adaptor Lat do not participate in early T cell signaling events. *Nat. Immunol.* 12:655–662. http://dx.doi.org/10.1038/ni.2049